Raman and Nuclear Resonant Spectroscopy in Geosciences

Jung-Fu Lin

Department of Geological Sciences, The University of Texas at Austin, Austin, TX, USA

Ercan E. Alp

Advanced Photon Source, Argonne National Laboratory, Argonne, IL, USA

Alexander F. Goncharov

Geophysical Laboratory, Carnegie Institution of Washington, DC, USA

ABSTRACT

Herein is presented a review of recent technical advances in Raman and nuclear resonance spectroscopy (both Mössbauer spectroscopy and nuclear resonant inelastic X-ray scattering spectroscopy (NRIXS)), as they have great implications for geoscience. Optical and X-ray spectroscopies probe different momentum and energy transfers caused by interactions between the incident light and the lattice, making them complementary and applicable to numerous scientific applications. Raman spectroscopy measures the optical vibrational modes at infinitely small momentum transfer whereas Mössbauer spectroscopy imparts negligible momentum transfer but can distinguish hyperfine interactions (quadrupole splitting, chemical shift, and magnetism) with neV energies. NRIXS measures the phonon density of states, which can be used to derive vibrational, thermodynamic, elastic, and electronic properties of the materials. Raman spectroscopy provides valuable and easily interpretable information about material properties using a

number of experimental platforms such as noninvasive tomographic imaging of minerals with sub-micrometer spatial resolution, *in situ* studies under extreme conditions of high pressure and temperature (*P*-*T*), and as a remote mineralogical and organic/biological probe for planetary exploration missions. The advent of synchrotron Mössbauer and NRIXS experiments provides a unique capability to probe the properties of iron-containing minerals that exist in the Earth's interior at high *P*-*T* conditions, as well as materials from the surface of Mars and the Moon. These recent and exciting developments have become possible because of the availability of dedicated synchrotron radiation beamlines, and the successful operation of two miniaturized Mössbauer spectrometers on the surface of Mars. The techniques addressed here permit the study of vibrational, electronic, elastic, and thermodynamic properties of planetary materials under variable thermodynamic conditions, making them highly valuable in geoscience implications.

1. INTRODUCTION

The advent of synchrotron X-ray and optical laser sources has had profound implications in understanding properties of geological and planetary materials under variable pressure-temperature (*P*-*T*) and compositional environments (McMillan, 1989; Alp *et al.*, 2011). In this article, we have critically examined the technical and scientific aspects of vibrational spectroscopy using Raman and nuclear resonance spectroscopy excited with synchrotron radiation (both synchrotron Mössbauer spectroscopy (SMS) and nuclear resonant inelastic X-ray scattering (NRIXS)). These techniques each carry unique, complementary capabilities that permit the study of vibrational, electronic, elastic, and/or thermodynamic properties of planetary materials under a wide range of thermodynamic conditions (e.g., Goncharov *et al.*, 2000, 2009; Lin *et al.*, 2005a,b, 2009; Alp *et al.*, 2011). Energy (or frequency) and momentum (or wavevector) transfers between incoming and scattered X-ray or laser sources categorize the techniques (**Section 1.2**) into ranges that provide probing access to many properties in planetary materials. In particular, the tightly focused X-ray and laser beams with extremely high fluxes now make it possible to study micro-sized geological materials with a dilute amount of elements of interest. These studies afford important clues about the local atomic arrangement, the strength of the chemical bonds related to forces acting on a particular atom of interest, and the effect of ligands on the overall lattice dynamics. We will first address the related perspective of these techniques in **Section 1**, discuss the application of the Raman technique in **Section 2**, focus on the application of the SMS and NRIXS techniques in **Section 3**, and elaborate on prospective directions in **Section 4.**

1.1 INTERACTION OF ELECTROMAGNETIC WAVES AND MATTER

The interactions between electromagnetic waves and matter, which result in a change in the wavevector ($\boldsymbol{k_0}$) and frequency ($\boldsymbol{\omega_0}$) of the incident light source, help to place the aforementioned spectroscopic techniques into scientific perspective. The change in frequency ($\Delta\boldsymbol{\omega}$) can be expressed as the energy change ($\Delta\boldsymbol{E}=\boldsymbol{h}\Delta\boldsymbol{\omega}$) between the incoming and exiting photons, whereas the wavevector difference ($\Delta\boldsymbol{k}$) represents the change in momentum ($\Delta\boldsymbol{Q}=\Delta\boldsymbol{k}$) (McMillan, 1985; Hawthorne, 1988) (Figure 1). In a lattice, the vibration of each atom about its equilibrium position is influenced by the vibrational motion of its neighbors through the interatomic potentials and symmetry of the lattice. Since the atoms are arranged in a periodic pattern (local, short-range, or long-range order), the lattice vibrational modes take the form of displacement waves travelling through the crystal (Kittel, 1996). These lattice waves may be described as longitudinal or transverse acoustic waves. The nuclear displacements result in an oscillating dipole moment, which interacts with the electromagnetic waves from either a laser or X-ray source, giving rise to particle-like phonons with discrete, quantized energies. In these long-wavelength lattice vibrations, the vibrations with adjacent cells are essentially in phase, so the number of vibrational modes that may be observed in Raman or infrared spectroscopy is equal to $3\boldsymbol{n}$-3 optical modes, where $\boldsymbol{n}$ is the number of atoms in the primitive unit cell (Kittel, 1996). The number of active vibrational modes follows the selection rules as a direct result of the lattice symmetry, described in greater detail in **Section 1.3** (McMillan, 1985). At relatively lower frequencies, there are also three acoustic branches that are responsible for the propagation of sound waves through the lattice. At an infinite wavelength with $\boldsymbol{k}\approx0$ near the center of the Brillouin zone, the three

acoustic modes are standing (zero frequency) and correspond to the speeds of one longitudinal and two transverse acoustic waves, whereas the optical modes give rise to the infrared and Raman active vibrations for long wavelength modes with $\boldsymbol{k}\approx 0$ (Kittel, 1996) (detailed in **Section 2**).

The quantized phonons disperse from the center of the Brillouin zone with infinite small momentum-energy (***Q-E***) transfers to the boundary of the Brillouin zone with maximum ***Q-E*** transfers at $\pi/2\boldsymbol{a}$ where ***a*** represents the lattice constant (Kittel, 1996). These phonon dispersion curves display the momentum dependence of the phonon frequency, and thus contain specific information on the inter-atomic interactions in the solid and liquid states, which are critically needed to theoretically understand the nature of the matter. Projection of the angular-dependent phonon branches results in a projected phonon density of states (DOS), which describes the number of the phonon states per interval energy as a function of the phonon energy (Kittel, 1996; Sturhahn, 1995, 2001; Alp *et al.*, 2011) (see **Section 3** for details). Full DOS accounts for all possible phonon branches and contains critical information about the vibrational, elastic, and thermodynamic properties of the matter. The phonon DOS is an important quantity in thermodynamics, as many intrinsic material parameters like vibrational specific heat, entropy, and internal energy are additive functions of the phonon DOS in the harmonic approximation and can be derived from the measured phonon DOS (see **Section 3** for details) (Sturhahn, 1995, 2001; Alp *et al.*, 2011).

1.2 GENERAL RAMAN AND NUCLEAR RESONANT SPECTROSCOPY

Considering ***Q-E*** transfers in terms of the interactions between the incident light and the lattice can be used to place Raman spectroscopy, SMS, and NRIXS into scientific perspective with respect to other spectroscopic methods that yield related information (Figure 1) (Calas and Hawthorne, 1988; Alp *et al*., 2011). Different domains of ***Q-E*** transfer can be accessed using unique spectroscopic probes employing various incident radiation sources such as electron, laser light, and synchrotron X-ray, each with different corresponding energies and energy resolutions. Accordingly, NRIXS probes energy transfers in the order of hundred meV and momentum transfers of approximately 0.1-10 nm^{-1} that arise from the phonon dispersions of the selective isotope in the lattice. SMS accesses the extremely low energy-momentum transfer domain and is uniquely sensitive to probing magnetism, electronic valence and spin states, and structural distortions (see **Section 3**). SMS provides the possibility to measure hyperfine interactions leading to chemical shift (**CS**), quadrupole splitting (**QS**), as well as magnetic hyperfine field and its direction (Mössbauer, 1958; Bürck *et al.*, 1992). NRIXS, on the other hand, measures lattice dynamics related quantities like recoil-free fraction or Lamb-Mössbauer factor (f_{LM}), phonon DOS, speed of sound, and all the thermodynamic quantities that are associated with the DOS, including vibrational specific heat, kinetic energy, Helmholtz free energy, interatomic force constants, and directional dependence of vibrational amplitudes in single crystals (Sturhahn, 1995; Sage *et al.*, 2001). The NRIXS can be considered as a complementary probe to inelastic neutron and X-ray scattering (Figure 1).

Optical Raman spectroscopy relies on coupling between the probing light and particular atomic vibrational motions through a change in polarizability, and does not

have enough momentum carried by the probing radiation (McMillan, 1985; Hawthorne, 1988). Therefore, the techniques can be used to measure the vibrational optical modes at the center of the Brillouin zone, even though the dispersive behavior cannot be directly observed (Figure 1).

1.3 ELECTRONIC STRUCTURES AND CRYSTAL FIELD THEORY

Describing the spectroscopic observations of the interactions between the lattice and the incident X-ray or optical radiation is greatly simplified by exploiting the symmetry of the lattice. As an example, for a molecular crystal with $\boldsymbol{m}$ molecules in a unit cell and $\boldsymbol{n}$ atoms in each molecule, the whole number of vibrational modes is $\boldsymbol{3mn}$. The number of observed optical vibrational modes is typically less than this number because of the energetic degeneracy caused by equivalency in the lattice symmetry or simply by inactive modes (McMillan, 1985; Hawthorne, 1988). In general, the symmetry of the lattice is described in terms of a set of symmetry elements that follow the operations of group theory to express certain spatial relations between different parts of the lattice. The combination of these symmetry operations produces an irreducible representation that represents a pattern corresponding to changes in physical quantities compatible with symmetry of the crystal. The symmetry arguments can also be used to predict or rationalize the relative intensity and polarization dependence of the phonons associated with transitions between electronic states (McMillan, 1985).

Classically, crystal field theory (CFT) has been successfully used to describe the electronic structure of transition metal compounds with the positively charged metal cation and the negative charge on the non-bonding electrons of the ligand (Burns, 1993).

The metal's five degenerate *d*-orbitals experience specific energy changes upon being surrounded by certain symmetry of ligands, which act as point charges. In combination with molecular orbital theory, CFT can be transformed to ligand field theory (LFT), which allows for a better understanding of the process of chemical bonding, electronic orbital structure, and other characteristics of coordination complexes. All of this information is needed to have a comprehensive understanding of the experimental results from the Raman and NRS measurements.

Take for example an octahedron, in which six ligands, each positioned along a Cartesian axis, form an octahedral shape around the metal ion, such as the FeO_6 octahedron in the lower-mantle ferropericlase (Mg,Fe)O (Figure 2) (Lin and Tsuchiya, 2008a). Based on CFT (Burns, 1993), the *d*-orbitals of the metal Fe^{2+} ion in this complex split into two sets with an energy difference, Δ_o (the crystal-field octahedral splitting parameter). The d_{z2} and d_{x2-y2} orbitals lie along Cartesian axes and will therefore experience an increase in energy due to repulsion caused by their proximity to the ligands (Burns, 1993) (Figure 2). The d_{xy}, d_{xz} and d_{yz} orbitals do not lie directly along any Cartesian axis but lie instead in planes between the ligands and are thus lower in energy than the d_{z2} and d_{x2-y2}, actually being stabilized. The three lower-energy orbitals are collectively referred to as $\boldsymbol{t_{2g}}$, and the two higher-energy orbitals as $\boldsymbol{e_g}$. It should be noted, however, that the orbital splitting energies are directly related to the specific molecular geometry of the complex. Thus, a tetrahedral ligand arrangement causes the $\boldsymbol{t_{2g}}$ orbitals to be higher in energy than the $\boldsymbol{e_g}$ orbitals and has a crystal field splitting energy of Δ_t. The occupation of the 3*d* orbitals is defined by the surrounding environment of the iron atom and influenced by factors such as bond length, crystallographic site, pressure, and

temperature (some of these parameters can be interconnected). Under ambient conditions in silicates and oxides, it is energetically favorable for the 3*d* electrons to occupy different orbitals with the same electronic spin; that is, the high-spin state with four unpaired electrons and two paired electrons in Fe^{2+} (spin quantum number ($\boldsymbol{S}$) = 2), for example (Dyar *et al.*, 2006; Lin and Tsuchiya, 2008a). In this case, the hybridized $\boldsymbol{t_{2g}}$-like and $\boldsymbol{e_g}$-like orbitals of the six-fold coordinated iron are separated by the crystal field splitting energy (Δ_o), which is lower than the electronic spin-pairing energy (Λ). The crystal field splitting energy can be significantly influenced by the energy change associated with pressure, temperature, and/or composition (Burns, 1993). The increase of the crystal field splitting energy relative to the spin-pairing energy under high pressures can eventually lead to the pairing of 3*d* electrons of opposite spin; that is, the low-spin state with all six 3*d* electrons paired in Fe^{2+} ($\boldsymbol{S}$ = 0). The high-spin to low-spin pairing transition of Fe^{2+} has recently been observed to occur in ferropericlase and perovskite at lower-mantle pressures (e.g., Badro *et al.*, 2003, 2004; Lin *et al.*, 2005c). The scheme of the crystal field splitting energy relative to the spin-pairing energy, however, becomes rather complex through crystallographic site distortion and electronic band overlap where occupancy degeneracy may be lifted. In particular, the degeneracy of the electronic energy levels can be lifted through Jahn-Teller effect.

2. RAMAN SPECTROSCOPY

Raman spectroscopy is one of the most informative techniques in geo- and planetary science research, providing valuable and easily interpretable information about material properties using a number of experimental platforms. These include noninvasive

tomographic imaging of minerals with sub-micrometer spatial resolution, *in situ* studies under extreme high *P-T*, and as a remote mineralogical and organic/biological probe for planetary exploration. Raman spectroscopy allows for rapid *in situ* measurements that provide direct information about the bonding state of a material through the observations of elementary vibrational excitations -- the phonons (Born and Huang, 1954). Therefore, detailed studies of Raman spectra can be used for crystalline phase identification and structural analysis (McMillan *et al.*, 1996), detection of phase transformations (Raman and Nedungadi, 1940), measurements of melting curves (Goncharov *et al.*, 2008), as well as for the determination of elastic and thermodynamic properties (Merkel *et al.*, 2000). Moreover, excitations of magnetic origin can be detected, which provide information about the magnetic structure (e.g., related to the electronic spin state of Fe^{2+} in planetary materials) (see section **3.4.2**) and the nature of electronic correlations in strongly correlated materials (Goncharov and Struzhkin, 2003). Raman spectroscopy is well suited for ultra-high pressure studies when coupled with a diamond anvil cell (DAC) (Hemley and Porter, 1988), as diamond anvils are transparent in the visible and near infrared spectral ranges. This application to stressed diamond culets in the DAC serves as an effective and very convenient way of measuring pressures in the DAC (even at high temperatures), even if there is no other usable pressure sensor in the DAC cavity (e.g., Akahama and Kawamura, 2004). In addition, Raman pressure gauges (e.g. cBN or ^{13}C diamond) allow for pressure measurements in chemically reactive environments at high pressures and temperatures (e.g., Goncharov *et al.*, 2005a; Mysen 2010).

Raman spectroscopy is very complementary to X-ray spectroscopy (e.g., Mössbauer and NRIXS, see **Section 3**) in studies under extreme conditions, as it is applicable for

studies of low atomic number, amorphous, and heterogeneous materials (e.g., having microscopic chemically-reacted compounds). As such, Raman spectroscopy in combination with high-magnification microscopes (micro-Raman) has been a powerful tool for studying properties of complex rock assemblages containing very small fluid and solid inclusions. Owing to the exceptional phase selectivity of Raman spectroscopy, this technique has been used as a versatile and indispensible tool for planetary exploratory missions.

2.1 THEORY OF VIBRATIONAL PROPERTIES OF MOLECULES AND CRYSTALS

Raman scattering is an inelastic process that involves the interaction of an incoming photon with an elementary excitation in the probed material. In keeping with the laws of conservation of momentum and energy, the scattered photon loses (Stokes) or gains energy (anti-Stokes) that corresponds to the elementary excitation energy in the material (e.g., phonon energy). The wavevector direction of the detected photon is determined by the chosen direction of the incident laser beam and the direction of the scattered radiation. In the great majority of cases considered here, the wavevectors of the incident and scattered photons are opposite to each other in the "back-scattering geometry," allowing the same optics to be used for both excitation and collection. Following the selection rule of the wavevector for the Raman processes, the energy transfer of the measured phonons is of the order of the wavevector of the exciting laser, which is about 10^5 cm^{-1}. This corresponds to phonons near the Brillouin zone center, though zone boundary phonons usually have wavevectors at around 10^8 cm^{-1} (Figure 1).

The Raman scattering cross-section depends strongly on the phonon (vibrational) mode coordinate that is normal to the wavevector of vibrational motion, corresponding to the normal mode. Raman-active modes correspond to normal modes for which the change in polarizability, $\boldsymbol{\alpha}$ (ability to redistribute electrons in response to the external electric field, $\boldsymbol{E}$, and to produce the dipole moment), of the system is nonzero $\Delta \boldsymbol{Q} > 0$. This modulation of the polarizability creates light scattering on modified frequencies (beats). The normal mode is Raman active if the transition moment integral $\int \psi_v^i \alpha \psi_v^f \, d\tau$ (ψ_v^i and ψ_v^f are the elecronic wavefunctions corresponding to the initial and the final states, respectively) is nonzero. This determines that the Raman-active modes must have symmetry of $\boldsymbol{\alpha_{ij}}$ or squares of coordinates (*xx, xy*, etc). Thus, these modes can be determined from the irreducible representation of the crystal symmetry point group (Fateley *et al.*, 1972) and can be identified by analyzing the polarization properties of the incident and scattered beams (Porto *et al.*, 1967). As Raman and infrared spectroscopy (Lu *et al.*, 1999) have different selection rules, they are often complementary.

The normal modes in molecular crystals (which are of interest for this chapter) can be classified as intra- and intermolecular; this works most accurately in the weak coupling regime, for which the difference between the two is large (Zallen, 1974). For a molecular crystal with $\boldsymbol{m}$ molecules in a unit cell and $\boldsymbol{n}$ atoms in each molecule, the whole number of vibrational modes is $\boldsymbol{3mn}$. Out of these, three are acoustic modes that cannot be observed in Raman processes as they have very low frequencies near the Brillouin zone center and should be studied by Brillouin spectroscopy (Gillet *et al.*, 1998) (Figure 1). Thus, the $\boldsymbol{3mn-3}$ optical modes are divided between intermolecular translational ($\boldsymbol{3m-3}$), free and/or restricted molecular rotations ($\boldsymbol{mN_{fr}}$, where $\boldsymbol{N_{fr}}$ is the number of rotational

degrees of freedom of the molecule), and the intramolecular vibrations or fundamentals ($N_f = 3mn\text{-}3m\ \text{-}mN_{fr}$).

The symmetries of these modes (and therefore their activities in either Raman or infrared) can be obtained using group theory. A technique called the correlation method uses a correlation of the site group symmetry for each atom (or molecule) to the factor group (symmetry of the crystal) (Fateley *et al.*, 1972). These correlations can be performed for each atom and for each structural group (e.g., molecule), thus giving the irreducible representations for each kind of intra- and intermolecular vibration. The group theory analysis becomes more complex in the case of a molecular solid that has orientationally disordered phases such as δ-N_2 (Schiferl *et al.*, 1985). In this case it is necessary to correlate the irreducible representations of the molecular, site, and crystal group symmetries.

2.2 INSTRUMENTATION FOR RAMAN EXPERIMENTS

Advanced Raman instrumentation typically enhances the sensitivity (e.g., surface-enhanced Raman) (Brown and Dlott, 2009), improves the spatial resolution (Raman microscopy), or increases the ability to acquire very specific information (resonance Raman). Raman spectroscopy has experienced dramatic technical improvements due to the development of extremely sensitive array detectors, such as the charge coupled device (CCD), fast imaging spectrometers, and effective optical components (e.g., Turrell *et al.*, 1996; Gillet *et al.*, 1998). CCD detectors are extremely efficient throughout the visible and near infrared spectral range, due to their high quantum efficiency (QE) (as high as 95% QE in commercial CCDs) and extremely low dark current level. The CCD detectors are

further improved by the development of the new electron multiplying CCD (EMCCD) and the elimination of "etalon effects" from unwanted fringes of constructive and destructive interference, which can artificially modulate a Raman spectrum in the near IR spectral range. The EMCCD detectors are ultra-sensitive to light, thus allowing the study of very weak Raman signals using photon counting and multiplying technique. Intensified CCD (ICCD) detectors with gated capabilities serve in a variety of applications to improve the signal-to-noise ratio (Dussault and Hoess, 2004) or to facilitate measurements of time resolved spectra.

The development of volume holographic (transmission) gratings (VHG) has changed Raman instrumentation over last 1-2 decades substantially (Kim *et al.*, 1993). First-generation VHG was based on holographic technology using thin polymeric materials (Yang *et al.*, 1991; Tedesco *et al.*, 1993). Notch filters, which are built using the VHG technology, efficiently block undesirable Rayleigh-scattered light, obviating the need for cumbersome low-transmission double subtractive monochromatic and filtering systems for routine measurements above 50 cm^{-1}. These advances in Raman spectroscopy have made the method easier and more applicable to routine problems, such as those in industrial laboratories. More recently, new hard-coated optical filters (Erdogan and Mizrahi, 2003), which have a comparable transition width with those manufactured using a holographic technology, have appeared on the market. Moreover, a new generation of notch and bandpass filters with a transition width as narrow as 10 cm^{-1} has been developed recently based on solid state technology (Moser and Havermeyer, 2009). They are expected to be much more environmentally stable, and have shown no degradation over time.

2.2.1 RAMAN MICROPROBE AND MAPPING

The Raman microprobe uses a 3D mapping technique and deals with the natural or quenched sampled after high *P-T* experiments. In the case of samples at ambient *P-T* conditions, one can use an objective lens with a large numerical aperture, as the distance to the sample can be extremely short. This makes possible 3D Raman tomography of the sample with sub-micrometer spatial resolution. For example, with a 100X N.A.=0.8 objective lens, the typical lateral spatial resolution is in the order of submicrons, and the depth resolution can about 1 μm (Steele *et al.*, 2007; Kaminsky *et al.*, 2009). The instrumentation for this technique includes a confocal Raman microscope coupled to a motorized computer controlled X-Y-Z sample stage. Sample preparation (Fries and Steele, 2011) is very straightforward, and measurements can be performed on whole rock specimens through selecting a flat, polished section, thin polished sections, or even by using a powdered sample. Optically polished surfaces maximize the signal and the spatial resolution.

Confocal Raman imaging under extreme conditions (e.g., in DAC) has not been realized yet. The newly designed laterally supported diamond anvils (Boehler and De Hantsetters, 2004) allow for the use of objective lenses with much larger numerical aperture (e.g., NA=0.7) than with the anvils of conventional design, making high *P-T* 3D Raman mapping principally possible.

2.2.2 RAMAN SPECTROSCOPY IN HIGH *P-T* DAC

Pressure substantially affects the properties of the planetary materials and of the diamond anvils in the DAC; therefore, the instrumentation required needs to be more flexible. Raman spectroscopy under simultaneous conditions of high *P-T* was in its infancy until quite recently (Gillet *et al.*, 1998) when a CO_2 laser with a wavelength of 10 μm was introduced as the laser heating source (Gillet *et al.*, 1993; Tschauner *et al.*, 2001). One limitation to achieving high pressure is sample dimension because the typical laser spot diameter is about 30 μm. Additionally, this technique is limited to the materials that have a strong absorption in the spectral range of the CO_2 laser. Most of the earth minerals have phonon absorption bands in this spectral range. However, planetary materials such as ices and hydrogen do not absorb the CO_2 laser radiation well, with the exception of H_2O at high pressures (Asahara *et al.*, 2010).

Use of near IR lasers (e.g., with a wavelength of 1060 nm) as a heating source reduces the heating spot to the order of microns and produces more stable heating conditions. A thin foil with a small hole(s) or powder made of chemically stable metals (e.g., Pt) can serve as a laser beam absorber thereby producing high-temperature conditions for the surrounding sample material (Lin et al., 2004a; Goncharov and Crowhurst, 2005). Finite elemental calculations (Subramanian *et al.*, 2011) performed in the sample cavity, with the realistic experimental geometry and thermochemical parameters for the sample and other surrounding materials, show that the temperature gradients in a hole of the metallic coupler are relatively small near the geometrical center (Figure 3). Thermal insulation layers near the diamond anvil tips reduce the heat flow from the sample areas thereby minimizing the temperature gradients across the sample.

These temperature gradients can be reasonably small (<15%), enabling studies of the phase diagrams at high *P-T* conditions, including melting curves.

The system built at the Geophysical Laboratory at the Carnegie Institution of Washington (GL CIW) (Figure 4) combines double-sided laser heating with a Raman system (Lin *et al.*, 2004a; Goncharov *et al.*, 2009). A Mitutoyo near IR 20X long-working distance lens focuses the IR radiation on the sample and collects Raman spectra in the backscattering geometry. The single-frequency solid-state 458 and 488 nm lasers, with maximum powers of 300 and 100 mW, respectively, are used as a Raman excitation source. A continuous-wave Yb fiber laser with a maximum laser power of 200 watts is used as the heating source, and is introduced into the Raman system using a polarizing beam-splitter cube and focused to a 15-20 μm spot. The heating laser power is increased in steps (by rotating a λ/2 wave plate coupled to a polarization cube). The system is equipped with laser beam shaper, which makes a flat laser beam top similar to the X-ray diffraction laser heating system (Prakapenka *et al.*, 2008). It has been recently automated for data acquisition, which includes performing all the spectral measurements at variable heating laser power (Subramanian *et al.*, 2010); this upgrade saves up to 90% of the time spent compared to manual data acquisition.

Continuous Raman excitation, using a spatial filter and incident laser at 458 nm, allows one to suppress the thermal radiation emitted by the sample and the coupler, sufficiently obtaining high quality Raman spectra up to approximately 2000 K (Goncharov and Crowhurst, 2005). At higher temperatures, when thermal radiation rises above a critical threshold and obscures the Raman signal, a pulsed Raman system with 532 nm excitation synchronized with the gated intensified CCD detector (Goncharov and

Crowhurst, 2005; Shim *et al.*, 2005), in combination with continuous (Goncharov *et al.*, 2008) or pulsed laser heating (Goncharov *et al.*, 2009) can be used. As the detector collects the whole Raman signal during the relatively short gate time and is closed between pulses, any continuous (or longer lasting) spurious radiation is suppressed; the magnitude of the suppression is proportional to the ratio of the pulse interval to the gate width. Suppression factors of up to 50,000 have been reported (Goncharov and Crowhurst, 2005), providing the possibility to acquire Raman signals at temperatures exceeding 5,000 K.

2.2.3 RAMAN INSTRUMENTATION FOR PLANETARY EXPLORATION

Raman spectroscopy has been proposed as a tool for analytical systems used in missions to Mars and, more recently, as a potential mineralogical probe for missions to Venus (e.g., Clegg *et al.*, 2009; Wang, 2009). Indeed, only Raman spectroscopy and X-ray diffraction can definitively identify nearly all crystalline minerals based upon unique narrowband features (Blacksberg *et al.*, 2010). The Raman technique is intended to acquire mineralogical, biological, and elemental information on planetary surfaces for lander/rover types of planetary missions. Small portable remote Raman systems have been shown to be effective in identifying hydrous and anhydrous minerals, glasses of mineral compositions and ices.

The principle of background suppression has been applied for remote Raman spectroscopic instrumentation (Misra *et al.*, 2005; Blacksberg *et al.*, 2010). Recent studies (Sharma *et al.*, 2010) show that high-quality Raman spectra of minerals and volatiles (supercritical CO_2) at high temperatures (up to 1003 K) can be obtained using a

telescopic optical system from distances of up to 9 meters even in the presence of the thermal radiation, fluorescent, and natural daylight backgrounds. Other technical aspects of building Raman micro-spectrometers for planetary missions are discussed in great detail by Tarcea *et al*. (Tarcea *et al.*, 2008).

2.3 RAMAN ANALYSES OF PLANETARY MATERIALS

Raman spectroscopy can be applied towards analyses of the phases presented in natural or synthesized materials under controlled *P-T* conditions (McMillan *et al.*, 1996). This has been practiced in conjunction with geological field studies and experimental petrology. Moreover, Raman spectroscopy can be applied to *in situ* study during the rover planetary missions for on-surface planetary mineralogy to study meteorites (Fries and Steele, 2008) and for samples recovered from other planetary bodies such as the moon (Steele *et al.*, 2010). Laboratory studies under extreme *P-T* conditions serve as an important guide to understand material behavior in planetary interiors. This information combined with theoretical calculations and seismological and planetary observations provide an input for planetary modeling.

2.3.1 PHASE IDENTIFICATION IN NATURAL AND SYNTHETIC SAMPLES

Micro-Raman studies, and especially Raman micro-tomography, can provide important constraints on *P-T* conditions encountered by rocks, particularly during metamorphism as different polymorphs of minerals have characteristic Raman spectra (McMillan *et al.*, 1996). Raman microscopy provides unambiguous identification of the minerals and their textures, as the selectivity in these observations is very high due to the

strict Raman selection rules and to the presence of vibrational frequencies in the "fingerprint regions." Raman confocal microscopy is an essential tool used to study fluid inclusions as it provides valuable information about the melting points and physical behavior of rocks in Earth's deep crust or even in the mantle (Anderson and Neumann, 2001; Fries and Steele, 2011). Moreover, Raman spectroscopy is extremely informative for investigations of carbonaceous matter in earth materials and meteorites (Fries and Steele, 2011). Here we briefly review some representative examples from recent studies.

Katayama *et al*. have found that zircon preserves multiple mineral inclusions including very high-pressure phases such as diamond and coesite (Katayama and Maruyama, 2009). Analyses of mineral compositions in inclusions preserved in zircon constrain the metamorphic *P-T* conditions and provide the timing of each stage of the complex metamorphic history of rocks at high *P-T* conditions. Bauer *et al*. have used Raman spectroscopy as a nondestructive tool to study the composition of multiple inclusion phases in zircon and to determine the age of the high-temperature metamorphic event (Bauer *et al.,* 2007).

A rare phase of hydrous aluminium silicate (Wirth *et al.*, 2007), and nyerereite and nahcolite (Kaminsky *et al.,* 2009) have been identified as micro- and nano-inclusions in diamond from the Juina area, Brazil. Sobolev *et al*. determined an initial pressure of Venezuela diamond formation based on the Raman frequency of a coesite inclusion (Sobolev *et al.*, 2000).

Nestola *et al.* have performed a combined single-crystal X-ray diffraction and Raman study of an olivine inclusion in diamond from Udachnaya kimberlite, Siberia (Nestola *et al.*, 2011). The internal pressure of the olivine inclusion and the diamond formation

pressure were determined. Likewise, Yasuzuka *et al.* determined the Mg composition and pressure of an olivine inclusion in diamond based on the calibration obtained from the Raman study of synthetic and natural materials with different Mg composition at high pressures using the DAC (Yasuzuka *et al.*, 2009). Based on the magnitude of the Fermi diad splitting in the Raman spectra of CO_2 fluid inclusion, Yamamoto *et al*. determined the depth origin of ultramafic-mafic xenoliths from the deep Earth (Yamamoto *et al.*, 2007).

2.3.2 RAMAN MICROPROBE STUDY OF METEORITES AND LUNAR SAMPLES

Raman can also be used in studies aimed at the search for life or evidence of past extraterrestrial life. For example, Steele *et al.* performed a detailed Raman tomography study of a carbonate globule from a Martian meteorite (Steele *et al.*, 2007). Macromolecular amorphous carbon was found in association with magnetite in these meteorite samples. The authors propose that these results represent experimental evidence for the synthesis of abiotic Martian carbon. Steele *et al.* also report on the detection of discrete multiple micrometer-sized graphite phases (graphite whiskers) within Apollo 17 impact breccias (Steele *et al.*, 2010). This study indicates that impact may be a process by which such unusual form of carbon can be formed in our solar system.

2.3.3 LABORATORY STUDIES AT HIGH *P-T*

Raman spectroscopy has been used to investigate volatiles (e.g., H_2, H_2O, CO_2, CH_4) in the resistively and laser heated DAC up to 150 GPa and 3000 K, as they can be

abundant volatile components in planetary interiors. The results for CO_2 and CH_4 show a lot of complexity such as rich phase diagrams and chemical reactivity under extreme *P-T* conditions (Benedetti *et al.*, 1999; Iota *et al.*, 1999; Gregoryanz *et al.*, 2003; Goncharov *et al.*, 2005a,b; Lin *et al.*, 2005a; Zerr *et al.*, 2006; Eremets and Trojan, 2009; Hirai *et al.*, 2009; Kolesnikov *et al.*, 2009; Subramanian *et al.*, 2011). One of the major questions about the high *P-T* behavior of CO_2 is: does it form a framework structure analogous to six-fold coordinated SiO_2 stishovite (Hemley, 2000). Based on *in situ* X-ray diffraction and Raman spectroscopy measurements above 30 GPa and 1500 K, carbon dioxide is reported to transform to a polymeric form with fourfold coordinated carbon atoms, named phase V (Iota *et al.*, 1999; Yoo *et al.*, 1999; Santoro *et al.*, 2004). At lower temperatures and above 50 GPa, the molecular form of CO_2 was reported to transform to phase VI (Iota *et al.*, 2007) and an amorphous form (Santoro *et al.*, 2006). Initially, the six-fold stishovite-like CO_2 was considered compatible with experimental results for both. The model for the six-fold coordination of the amorphous form and the phase VI, together with their similarity with SiO_2, were later questioned. Mixed coordination models for the amorphous phase and the presence of local mechanical instabilities in six-fold coordinated structures have been further proposed (Montoya *et al.*, 2008).

The speciation of carbon in the Earth's interior is critical for understanding the origin of petroleum (Scott *et al.*, 2004). Formation and stability of methane under conditions corresponding to the Earth's upper mantle have been demonstrated in recent years (Kenney *et al.*, 2002; Scott *et al.*, 2004; Chen *et al.*, 2008). However, the formation of heavier alkanes remains unclear and controversial. Shock-wave experiments (Nellis *et al.*, 1981; Nellis *et al.*, 2001) suggest the decomposition of methane into molecular H_2 and

carbon, with precipitation of diamond (Ross, 1981). In contrast, theoretical calculations indicate the presence of saturated hydrocarbons before complete dissociation into diamond and hydrogen (Ancilotto *et al.*, 1997; Kress *et al.*, 1999). Earlier DAC experiments do not support the formation of alkanes (Culler and Schiferl, 1993; Benedetti *et al.*, 1999; Hemley and Mao, 2004; Zerr *et al.*, 2006; Chen *et al.*, 2008), but indicate the dissociation of methane to atomic carbon in the form of diamond (Benedetti *et al.*, 1999; Zerr *et al.*, 2006) or soot (Culler and Schiferl, 1993; Hemley and Mao, 2004), molecular hydrogen (Hemley and Mao, 2004; Zerr *et al.*, 2006), and other unidentified hydrocarbons (Benedetti *et al.*, 1999; Hemley and Mao, 2004; Chen *et al.*, 2008). Recent works in the laser heated DAC show a possibility of the formation of heavier hydrocarbons from methane at *P-T* conditions above 1000 K and 3 GPa (Hirai *et al.*, 2009; Kolesnikov *et al.*, 2009) (Figure 5). Moreover, these reactions have been shown to be reversible and can proceed under the oxygen fugacity conditions representative of the Earth's upper mantle. Recent theoretical calculations (Spanu *et al.*, 2011) support this chemical reactivity, but suggest more extreme *P-T* conditions for the chemical reaction forming heavier hydrocarbons.

3. SYNCHRTRON MÖSSBAUER SPECTROSCOPY AND NUCLEAR RESONANT INELASTIC X-RAY SCATTERING

Mössbauer spectroscopy (MS) is a versatile, useful technique commonly exploited in mineral physics, geophysics, and geochemistry, among other fields. By measuring the changes in the nuclear wave function as a result of changing surrounding electronic structure, MS can reveal information about electronic valence and spin states, ligand

symmetry, magnetism, and lattice dynamics. The Mössbauer effect, named after discoverer R. L. Mössbauer (Mössbauer, 1958), is described as resonant absorption and emission of gamma rays in a solid. MS has become a very common technique in geoscience due to the relatively modest amount of equipment needed, and because of its applicability to more than a dozen isotopes suitable and relevant to geological issues. These include the 3*d* transition metals (Fe, Ni, Zn), some elements (Ru, Sn, Sb and Te), rare earth elements (Sm, Eu, Dy, Tb, Er, Tm, Yb, and Gd), several actinides (Th and U), noble gases (Kr and Xe), and alkaline metals (K and Cs). For a complete list of Mössbauer active isotopes and their properties, see recently updated information provided by the Mössbauer Effect Data Center (Table 1) (see http://www.medc.dicp.ac.cn/Resources.php).

One of the very first applications of the Mössbauer effect was to measure the isomer shift of ^{57}Fe as a function of pressure, which is related to the change in the average value of 4*s* electron wave function density at the nucleus. This is a direct measure of the compressibility of the electron gas under pressure (Pound *et al*., 1961). Since then, the Mössbauer effect has been used to characterize minerals in terms of valence and spin states, magnetism, and crystal structure. There are a number of books and recent review articles that extensively address this subject (Greenwood and Gibb, 1972; Shenoy and Wagner; 1978; Long and Grandjean, 1989; Chen and Yang, 2007). More recent and exciting developments include the availability of dedicated synchrotron radiation beamlines, and the successful operation of two miniaturized Mössbauer spectrometers on the surface of Mars, which have been taking data since 2007. This planetary mission provided proof for the presence of deposits of carbonate minerals on the Martian surface

in situ (Morris *et al.*, 2010), and gave information about the mineralogy and distribution of Fe in Fe-bearing phases, including their oxidation states (Klingelhöfer *et al.*, 2003).

3.1 MÖSSBAUER EFFECT AND MÖSSBAUER SPECTROSCOPY

By compensating with small amounts of energy for changes in the sample due to hyperfine interactions, recoilless emission of gamma rays from a radioactive source and the subsequent resonant absorption can be accomplished. Of course, this interaction is accompanied by a number of concurrent or sequential processes involving X-ray absorption and fluorescence, Compton scattering, Auger electrons (due to internal conversion), and inelastic scattering. However, these processes are well understood, and can be differentiated by using time and energy discrimination techniques. The information in a measured Mössbauer spectrum includes the following: isomer shift, quadropole splitting, magnetic hyperfine splitting, and recoil-free fraction.

3.1.1 CHEMICAL SHIFT

Chemical (isomer) shift is due to a change in the energy level of the first nuclear excited state compared to that of the parent radioactive source, and is mainly caused by a change in the valence, pressure or temperature. It is expressed in units of the Doppler shift velocity applied to the emitting source or absorber, $\delta = \frac{v}{c} E_\gamma$, where **v** is the velocity, ***c*** is the speed of light, and $\boldsymbol{E_r}$ is the transition energy of the radioactive decay. This measurement can be related to changes in the electron density on the nucleus as follows: $\delta = C \times \left[\left|\psi_s(0)_{absorber}\right|^2 - \left|\psi_s(0)_{source}\right|^2 \right]$, where C is a constant and $\left|\psi_s(0)_{absorber}\right|^2$ is a

measure of the electron density on the nucleus in the absorber, not only due to *s*-electron population, but also due to changes in the other electronic levels, like *p*, *d*, or *f* electrons. A positive **δ** value indicates an increase in the *s*-electron density compared to that of the source. Since the source is always the same, this information can be used to classify different minerals and compounds, as well as the effects of applied pressures and temperatures. It should be noted that temperature dependence of the isomer shift should be corrected for second order Doppler shift. As shown in Figures 6 and 7, using Fe and Eu compounds as examples, the correlation between valence and isomer shift based on measured data provides a reliable fingerprint to distinguish between different mineral phases. For a more general reference of isomer shift, please reference a comprehensive treatise (Shenoy and Wagner, 1978).

3.1.2 QUADRUPOLE SPLITTING

Nuclei with a spin quantum number higher than ½ have non-spherical charge distribution, implying the presence of higher order terms and a multipole expansion into higher spherical harmonics. The presence of a nuclear quadrupole moment coupled with an electric field gradient is the origin of nuclear energy level splitting, which creates an opportunity for measurement using MS. The electric field gradient is a tensor, which can be defined along the direction of its highest value at the point of the absorbing nuclei. The strength of the interaction is then the product of the value of the quadrupole moment (a constant for each nuclei) and the field gradient, which depends on the crystal structure,ligand type, and orientation around the resonant nuclei. The strength of this interaction for an axially symmetric case is given by:

$$eQ = \int \rho r^2 \left(3\cos^2\theta - 1\right) d\tau$$

$$E_Q = \frac{e^2 qQ}{4I(2I-1)}\left[3I_z^2 - I(I+1)\right],$$

where ***eQ*** is the measure of the deviation from spherical charge distribution, ***eq*** is the maximum value of the electric field gradient, ***ρ*** is the charge density in a volume element ***dτ***, ***I*** is the nuclear spin operator, and $\boldsymbol{I_z}$ indicates the possible values in the presence of a field gradient. The origin of the field gradient is due to valence electrons and neighboring ions. The systematics of the quadrupole splitting may reveal a measure of the distortion around the resonant nuclei; thus, the presence or absence as well as the magnitude of the qaudrupole splitting is valuable information in understanding the electronic structures of interest.

3.1.3 MAGNETIC HYPERFINE SPLITTING

Since nuclei have spin, and hence nuclear magnetic moment, they will interact with a magnetic field, leading to nuclear Zeeman effect. The strength of this splitting is given by $E_{mag} = -\frac{\mu H m_I}{I}$, where ***μ*** is the nuclear magnetic moment, ***H*** is the magnetic hyperfine field, $\boldsymbol{m_I}$ is magnetic quantum number, and ***I*** is the spin state of the ground or excited state. The strength of the magnetic hyperfine field depends on both electronic and nuclear factors that may lead to a net spin density on the nucleus. While these factors are very important in understanding the presence and magnitude of the Zeeman effect, its measurability and ability to be systematized provide an invaluable selectivity to MS.

3.1.4 RECOIL-FREE FRACTION

The resonant absorption of gamma rays is the result of nuclear transitions between various nuclear energy levels without exchanging phonons. This "recoil–free" fraction is also known as the Lamb-Mössbauer factor (the LM factor), and is akin to the better known Debye-Waller factor, used in X-ray or neutron diffraction. Both are a measure of the stiffness of the lattice, and they are related to each other by:

$$f_{LM} = \left\rangle e^{i\mathbf{ku}} \right\langle^2 = e^{-k^2 \rangle x^2 \langle}$$

$$f_{DW} = \left\rangle e^{i\mathbf{qu}} \right\langle^2 = e^{-q^2 \rangle x^2 \langle}$$

$$\ln f_{DW} = \frac{q^2}{k^2} \ln f_{LM} \quad ,$$

where $\boldsymbol{k}$ is the total momentum of the resonant photon, and $\boldsymbol{q}$ is the transferred momentum of the photon in a scattering experiment, which depends on the scattering angle, $\boldsymbol{\theta}$, as follows: $q = 4\pi \sin\theta / \lambda$. These four quantities measured by MS form the basis for quantitative and qualitative characterization of many systems, including minerals.

3.2 MÖSSBAUER INSTRUMENTATION USING CONVENTIONAL AND SYNCHROTRON SOURCES

Laboratory-based Mössbauer spectrometers have been made commercially available by a number of instrument manufacturers. The instrumentation involves a velocity transducer to move the radioactive parent source to produce the required Doppler shift, and an absorber holder, which can be in a cryostat, furnace, magnet, high-pressure cell, or some combination of these (Figure 8). Modern Peltier cooled silicon detectors are replacing proportional counters because they provide a better energy discrimination,

approximately 2% as opposed to 15 %. The Mössbauer signal is amplified, sent to a pulse height analyzer for energy discrimination, and synchronized with the transducer wave generator in a multichannel scaler unit for velocity binning.

The synchrotron-based nuclear resonant studies, on the other hand, are more complex. The main components are shown in Figure 9. The Mössbauer "beamlines" involve standard X-ray optics components like monochromators, focusing mirrors, and detection electronics and signal processing units (Alp *et al.*, 1994). More recently, newer detection systems have been used to incorporate laboratory-based Mössbauer velocity drives into the beamline optics in an attempt to collect data in the traditional form, albeit with reduced efficiency (Seto *et al.*, 2009).

3.3 NUCLEAR RESONANT SCATTERING USING SYNCHROTRON RADIATION

Use of the synchrotron radiation to replace the radioactive parent isotope source was first suggested by S. L. Ruby (Ruby, 1974), and experimentally observed by E. Gerdau (Gerdau *et al.*, 1985). Since then, more than a dozen of these transitions have been observed, including Ta, Th, Kr, Fe, Eu, Sm, Sn, Dy, Hg, I, K, Te, Sb, Ni, Ge, given in the order of resonance energy (See Table 1). Currently, there are at least five different storage rings in the USA (the Advanced Photon Source, APS, Argonne, Illinois), France (European Synchrotron Radiation Facility, ESRF, Grenoble), Germany (Hasylab, PETRA-III, Hamburg), and Japan (Super Photon ring at 8 GeV, Spring-8, Hyogo and the National Laboratory for High Energy Physics, Accumulator Ring, KEK-AR, Tsukuba, Ibaraki). Two different types of experiments can be performed using the same optics: (1)

SMS (or nuclear forward scattering (NFS)) (Bürck *et al.*, 1992); (2) NRIXS (or nuclear resonant vibrational spectroscopy (NRVS), nuclear inelastic scattering (NIS) (Sturhahn *et al.*, 1995; Sage *et al.*, 2001).

An example of what can be learned from SMS and NRIXS data is given in Figure 10. SMS data yield the internal hyperfine field strength of phases typically found in meteorites, like kamacite (an iron-nickel alloy) and troilite (an iron-sulfur (FeS) compound). If needed, isomer shifts can also be measured by inserting a reference material into the beam before or after the sample. NRIXS data, on the other hand, provide vibrational information. The dynamical behaviors of atoms are at the core of understanding electronic, thermal and elastic properties of planetary materials and living organisms alike. Many of the elastic and thermal properties of materials depend on the distribution of the occupational states in various energy levels, as the atoms vibrate around their equilibrium positions. Well-known quantities like Young's modulus of elasticity, Grüneisen parameter, compressibility, specific heat, and thermal conductivity are a reflection of force constants acting between atoms. Modern computational methods like density functional theory (DFT) and its variants can make predictions about the forces holding materials together. However, all methods must be verified using experimental results from vibrational spectroscopy. Thus a number of techniques have been developed to study these properties. Among the photon-based probes, we can readily count Raman, Brillouin and infrared spectroscopy. However, some of these techniques have limited applicability and suffer from the fact that photon energies are very low, and carry very small momentum (Figure 1). Optical techniques like Raman and infrared spectroscopy work well when there is an optical mode in the right polarization to

couple to the incident light (see **Section 2**). Since the incident light is of very low energy compared to X-rays, there is not enough momentum transfer carried by the probing radiation. Hence, while the center-of-zone modes can be measured, their dispersive behavior inside the Brillouin zone cannot be observed (Figure 1). Also, these optical techniques are not element or isotope selective Table 1). The coupling strength is related to the polarizability generated by a particular mode. The NRIXS method overcomes many of these limitations: (1) It is element and isotope selective; (2) the incident X-rays carry large momentum, sufficient to integrate over the entire Brillouin zone; (3) peak intensities measured are directly related to the displacement of the targeted isotope; (4) for single crystals or oriented samples, the nuclear resonant probes are directionally sensitive. Here we highlight some of the relevant features of the NRIXS technique with an example as shown in Figure 10.

In terms of the instrumentation for NRIXS experiments, the synchrotron beam was monochromatized with a combination of diamond (111) double crystal monochromator and a nested pair of Si (4 0 0) and Si (10 6 4) reflections. The combination of these gave an overall resolution of 1.1 meV, with a flux of 6 GHz. A detailed description of high-resolution, tunable crystal monochromators was given earlier (Toellner, 2000). A silicon avalanche photodiode detector (APD) is used to detect scattered radiation as a function of energy around 14.4125 keV. The energy tuning is accomplished by tuning the inner Si (10 6 4) crystal across a total of 60 microradians for a scan of ± 90 meV while integrating the nuclear delayed signal between a 15 and 130 ns time window.

The phonon DOS, **g(E)**, is obtained from the single phonon excitation probability ($S_1(E)$) according to:

$$g(E) = \frac{E}{E_R}\tanh(\beta E)\left[S_1(E) + S_1(-E)\right],$$

where $\boldsymbol{E}$ is the relative energy of the incident photons with respect to the nuclear resonance energy, $\boldsymbol{E_R}$ is the recoil energy of the resonant nucleus, and $\boldsymbol{\beta}$ is the reduced temperature ($\boldsymbol{E/k_T}$). The phonon DOS is an important quantity in thermodynamics, because many intrinsic material parameters like vibrational specific heat, entropy, and internal energy can be derived from the measured phonon DOS. A computer program, PHOENIX, is used to evaluate the data and extract the above-mentioned thermodynamic quantities (Sturhahn, 1995, 2001).

Another important quantity that can be derived from the **g(E)** is the Debye sound velocity ($\mathbf{V_D}$) which is extracted from the lower region of the phonon DOS:

$$V_D = \left[\frac{M}{2\pi^2\rho\hbar^3}\frac{g(E)}{E^2}\right]^{1/3},$$

where $\boldsymbol{M}$ is the mass of the resonant nucleus, and $\boldsymbol{\rho}$ is the density. The initial curvature of the phonon DOS versus energy is related to the Debye sound velocity. Hence, a procedure has been developed to obtain this curvature with different upper bounds, in which a fit is made to extrapolate the Debye sound velocity. This quantity can be used to obtain compressional ($\boldsymbol{V_P}$) and shear ($\boldsymbol{V_S}$) wave velocities, provided that independent knowledge of bulk modulus ($\boldsymbol{K}$) and density ($\boldsymbol{\rho}$) is available under the conditions of each experiment, based on the following relationships (Mao *et al.*, 2001):

$$\frac{3}{V_D^3} = \frac{1}{V_P^3} + \frac{2}{V_S^3}$$
$$\frac{K}{\rho} = V_P^2 - \frac{4}{3}V_s^2 \quad .$$

One common misperception about nuclear resonance vibrational spectroscopy is that it only measures the properties of the nuclear resonant isotope. In reality, for low frequency vibrations, it has been demonstrated that all atoms move in unison, thus some of the most relevant properties like the sound velocity, extracted from the low-energy region of the density of states, is a reflection of the entire material (not of only the nuclear resonant element) (Hu *et al.*, 2003). This extension of application actually makes the approach more relevant to a large class of materials. Furthermore, through the use of the density functional theory (DFT), which is validated by NRIXS or NRVS, it is now possible to solve dynamical matrix and obtain a complete set of eigenvectors, at least for molecular crystals, like porphyrins or cubanes. Thus, for each mode, one can now determine the direction and amplitude of each atomic movement. Thus, even if the data is relayed to us by the nuclear resonant isotope of interest, the motion of all atoms in the lattice can be determined.

3.4 GEOPHYSICAL APPLICATIONS

For geophysical research, often one resorts to creating experimental conditions similar to the environments of the Earth's crust, mantle, transition zone, and outer and inner core. Since iron is the most abundant transition metal in all layers of the planet, the NRIXS and SMS experiments provide unique information on the planet at high *P-T* conditions. Today, it is possible to reach pressures above 370 GPa and temperatures of 5700 K using a laser-heated DAC (Tateno *et al.*, 2010). Even though there is a wide

range of geoscience applications for the NRIXS and SMS techniques, we will only focus on their implications in planetary interiors at high *P-T* (e.g., Lin *et al.*, 2004b, 2005b, 2007a,b; Zhao *et al.*, 2004).

3.4.1 SOUND VELOCITIES OF IRON ALLOYS BY NRIXS

The methodology of using Mössbauer nuclei as a probe of vibrational DOS has been successfully incorporated with the laser-heated DAC (Lin *et al.*, 2004b, 2005b; Zhao *et al.*, 2004), making it possible to measure the pressure-dependent V_D, V_P, and V_S at high *P-T*. This approach also opened the possibility of characterizing opaque samples like iron-containing alloys and ferropericlase (e.g., Jackson *et al.*, 2009). Since the technique is isotope selective through the Mössbauer nuclei, typical problems associated with sample environments leading to deteriorating signal-to-background ratio are readily avoided. By using a focused x-ray beam, and tunable high-resolution crystal monochromators with 1 meV resolution, partial phonon DOS is recorded for iron and a variety of iron alloys containing hydrogen (Mao *et al.*, 2004), carbon (Gao *et al.*, 2008), oxygen (Struzhkin *et al.*, 2001), sulphur (Kobayashi *et al.*, 2004; Lin *et al.*, 2004c), silicon and nickel (Lin *et al.*, 2003). Studies carried out up to 1700 K under pressure showed that high temperatures have a strong effect on the sound velocities of hcp-Fe at constant densities, leading to the re-evaluation of Birch's law (Lin *et al*., 2005b).

3.4.2 ELECTRONIC SPIN AND VALENCE STATES BY SMS

Mössbauer spectroscopy has proven to be very effective in the past in studying iron-bearing minerals. There is a large body of evidence that points out the relationship

between measured hyperfine interaction parameters and valence, spin, and magnetic states of iron and its compounds under ambient and extreme conditions. The use of the synchrotron radiation to excite Mössbauer transitions has further advanced the applicability of this technique to high-pressure studies due to an astonishing six orders of magnitude increase in the X-ray brightness when compared to lab-based radioactive sources.

Because of the partially filled *3d*-electron orbitals, the electronic valence and spin states of iron in the host lower-mantle phases can affect our understanding of a wide range of physical and chemical properties of the lower mantle (e.g., Lin and Tsuchiya, 2008a). Previous studies have shown that the spin transitions of Fe and variations in the Fe valence states can cause changes in density, elastic properties, electrical conductivity and radiative thermal conductivity of the lower mantle minerals. In particular, electronic spin-pairing transitions of iron that were proposed decades ago have been recently observed in the lower-mantle minerals including ferropericlase, perovskite, and possibly in post-perovskite at high pressures (e.g., Badro *et al.*, 2003, 2004; Li *et al*., 2004; Lin *et al*., 2005c, 2006, 2007). For example, the measured values of QS, ~0.8 mm/s, and CS, ~1.2 mm/s, from the Mössbauer spectra of the lower-mantle ferropericlase under ambient conditions are consistent with predominant high-spin Fe^{2+} in the octahedral coordination (Speziale *et al.*, 2005; Lin *et al.*, 2006). The simultaneous disappearance of the QS and the drop of the CS at approximately 60 GPa are consistent with a high-spin to low-spin electronic transition of iron in the ferropericlase (Speziale *et al.*, 2005; Lin *et al.*, 2006). The ratio of the high-spin to low-spin states of iron in ferropericlase as a function of

pressure can be derived from the modeling of the SMS spectra with the changes in the QS and CS values.

Iron exists in the Fe^{2+} and Fe^{3+} states in both perovskite and post-perovskite. Both Fe^{2+} and Fe^{3+} exist in the high-spin state in perovskite under ambient conditions. Most of the recent studies have observed extremely high QS values of the Fe^{2+} as high as ~4.4 mm/s in perovskite at high pressures (McCammon *et al.*, 2008; Lin *et al.*, 2008b). The relative area of the high-QS doublet increases with pressure at the expense of the low-QS doublet, and has been assigned as an intermediate-spin Fe^{2+} in the A site occurring at approximately 30 GPa (McCammon *et al.*, 2008). However, recent theoretical calculations support the notion that the extremely high QS site is a result of the atomic-site change rather than a high-spin to an intermediate spin transition (Bengtson *et al.*, 2009; Hsu *et al.*, 2010). At higher pressures, a new doublet component was assigned to the low-spin Fe^{2+} occurring at 120 GPa and high temperatures (McCammon *et al.*, 2010). Recent studies on Fe^{3+}-containing perovskite suggest that the Fe^{3+} in the octahedral B site undergoes a spin-pairing transition in perovskite, whereas Fe^{3+} in the A site remains high spin to at least 136 GPa (Catalli *et al.*, 2010).

Fe^{2+} likely exists in the bipolar-prismatic site with an extremely high QS of 3.8-4.5 mm/s and relatively high CS in post-perovskite, which has been assigned to the intermediate-spin Fe^{2+} state with a total spin momentum (*S)* of one (Lin *et al.*, 2008b; Mao *et al.*, 2010). However, theoretical calculations have found the intermediate-spin state unstable at lower-mantle pressures. Fe^{3+} exists in two different sites, the high-spin Fe^{3+} in the bipolar-prismatic site and the low-spin Fe^{3+} in the octahedral site. These site assignments indicate that the Fe^{3+} in the octahedral site undergoes a high-spin to low-spin

transition at high pressures through charge-coupled substitution. The formation of metallic iron and Fe^{3+} in post-perovskite is suggested to be achieved by self-reduction of Fe^{2+} to form iron metal and Fe^{3+}, similar to that in the perovskite (Jackson *et al.*, 2009). Since part of the interpretations for the Mössbauer results requires the knowledge for the total spin momentum of the 3*d* electronics in the samples, further integration of the Mössbauer results with other synchrotron X-ray spectroscopic results will be needed to better understand the spin and valence states of Fe in the deep Earth.

4. PROSPECTIVE DIRECTIONS

The techniques addressed here permit the study of vibrational, electronic, elastic, and thermodynamic properties of planetary materials under variable thermodynamic conditions, invaluably making them essential in geoscience implications. Prospective directions of the scientific quest here falls largely on new developments of these techniques that permit direct probe of these properties *in situ* statically or dynamically using advanced synchrotron light or optical laser sources and detecting techniques. Of particular interest is to develop new capabilities to probe material properties in extremely small quantity and extreme *P*-*T* environments that are beyond current reach but could potentially provide new insights into the planet as well as other planets and moons in the solar system.

Raman spectroscopy has improved dramatically over the last two decades, making previously challenging experiments routine. Increased sensitivity, for example, has allowed experiments to be carried out in a shorter amount of time with better spatial resolution. Moreover, portable and remote systems have become available, making use of

Raman spectroscopy for planetary missions quite feasible. There are prospects for further improvements of the spatial and temporal resolution of the Raman systems applied for geosciences. With regard to research using the DAC, developments have been seen in the submicron spatial resolution as a new capability for spectroscopic tomography in the DAC cavity. These will enable studies on the chemical reactivity on mineral interfaces as well as on heterogeneous samples of various forms, including the new capability of the surface enhanced Raman spectroscopy (SERS). The capabilities of time-resolved and pump-probe techniques remain to be further exploited, but the use of coherent anti-Stokes Raman spectroscopy (CARS) with the dynamic techniques can broaden geoscience applications. They can provide an access to studies of fast chemical reactivity and to more extreme *P*-*T* and stress rate conditions---all of great interest for planetary-earth sciences.

The advent of synchrotron Mössbauer and NRIXS experiments provides a unique capability to probe the properties of iron-containing minerals that exist in the Earth's interior at high *P*-*T* conditions, as well as materials from the surface of Mars and the Moon. These recent and exciting developments have become possible because of the availability of dedicated synchrotron radiation beamlines for studies under variable thermodynamic conditions, and the successful operation of two miniaturized Mössbauer spectrometers on the surface of Mars. There are, however, many other nuclear isotopes and their compounds that can be directly probed using the techniques, although technical developments in the X-ray optics and detectors for suitable transition energies are needed.

ACKNOWLEDGMENTS

The authors thank A. Wheat for editing the manuscript and are grateful to A. Steele for useful comments and suggestions. J.F.L. acknowledges financial support from NSF Earth Sciences (EAR-0838221 and EAR-1056670), Carnegie/DOE Alliance Center (CDAC), and Energy Frontier Research in Extreme Environments (EFree) Center. A. F. G. acknowledges financial support from NSF Earth Sciences (EAR-0842345 and EAR-1015239) Carnegie/DOE Alliance Center (CDAC), and Carnegie Institution of Washington.

REFERENCES

Akahama Y. and Kawamura H. (2004) High-pressure Raman spectroscopy of diamond anvils to 250 GPa: Method for pressure determination in the multimegabar pressure range. *J. Appl. Physics* **96**, 3748-3751.

Alp E. E., Mooney T. M., Toellner T., and Sturhahn W. (1994) Nuclear resonant scattering beamline at the Advanced Photon Source. *Hyperfine Interact.* **90**, 323-334.

Alp E. E., Sturhahn W., Toellner T. S., Zhao J., and Leu B. M. (2011) Nuclear resonance scattering of synchrotron radiation as a unique electronic, structural and thermodynamic probe (in submission).

Ancilotto F., Chiarotti G. L., Scandolo S., and Tosatti E. (1997) Dissociation of methane into hydrocarbons at extreme (planetary) pressure and temperature. *Science* **275**, 1288-1290.

Anderson T. and Neumann E. R. (2001) Fluid Inclusions in mantle xenoliths. *Lithos* **55** 301-320.

Asahara Y., Murakami M., Ohishi Y., Hirao N., and Hirose K. (2010) Sound velocity measurement in liquid water up to 25 GPa and 900 K: Implications for densities of water at lower mantle conditions. *Earth Planet. Sci. Lett.* **289**, 479-485.

Badro J., Fiquet G., Guyot F., Rueff J.-P., Struzhkin V. V., Vankó G., and Monaco G. (2003) Iron partitioning in Earth's mantle: toward a deep lower mantle discontinuity. *Science* **300**, 789-791.

Badro J., Rueff J.-P., Vankó G., Monaco G., Fiquet G., and Guyot F. (2004) Electronic transitions in perovskite: Possible nonconvecting layers in the lower mantle. *Science* **305**, 383-386.

Bengtson A., Li J., and Morgan D. (2009) Mössbauer modeling to interpret the spin state of iron in (Mg,Fe)SiO_3 perovskite. *Geophys. Res. Lett.* ***36***, L15301.

Bauer C., Rubatto D., Krenn K., Proyer A., and Hoinkes G. (2007) A zircon study from the Rhodope metamorphic complex, N-Greece: Time record of a multistage evolution. *Lithos* **99**, 207-228.

Benedetti L. R., Nguyen J. H., Wendell A. C., Liu H., Kruger M., and Jeanloz R. (1999) Dissociation of CH_4 at high pressures and temperatures: Diamond formation in giant planet interiors? *Science* **286**, 100-102.

Blacksberg J., Rossman G. R., and Gleckler A. (2010) Time-resolved Raman spectroscopy for *in situ* planetary mineralogy. *Appl. Optics* **49**, 4951-4962.

Boehler R. and De Hantsetters K. (2004) New anvil designs in diamond-cells. *High Pressure Res.* **24**, 391-396.

Born M. and Huang K. (1954) Dynamical Theory of Crystal Lattices. Oxford, Clarendon Press.

Brown K. E. and Dlott D. D. (2009) High-pressure Raman spectroscopy of molecular monolayers adsorbed on a metal surface. *J. Phys. Chem. C* **113**, 5751-5757.

Bürck U., Siddons D. P., Hastings J. B., Bergmann U., and Hollatz R. (1992) Nuclear forward scattering of synchrotron radiation. *Phys. Rev. B* **46**, 6207-6211.

Burns R. G. (1993) Mineralogical applications of crystal field theory. Cambridge University Press, Cambridge.

Calas G. and Hawthorne F. C. (1988) Introduction to spectroscopic methods. In *Review in Mineralogy: Spectroscopic Methods in Mineralogy and Geology* (ed. F. C. Hawthorne). Mineralogical Society of America, pp. 1-10.

Catalli K., Shim S. H., Prakapenka V. B., Zhao J., Sturhahn W., Chow P., Xiao Y., Liu H., Cynn H., and Evans W. J. (2010) Spin state of ferric iron in $MgSiO_3$ perovskite and its effect on elastic properties. *Earth Planet. Sci. Lett.* **289**, 68-75.

Chen Y. L. and Yang D. P. (2007) Mössbauer effect in lattice dynamics: experimental techniques and applications. Wiley-VCH Verlag GmbH & Co. KGaA, Weinheim, Germany, pp. 409.

Chen J. Y., Jin L. J., Dong J. P., and Zheng H. F. (2008) *In situ* Raman spectroscopy study on dissociation of methane at high temperatures and at high pressures. *Chinese Phys. Lett.* **25**, 780-782.

Chen J. Y., Jin L. J., Dong J. P., Zheng H. F., and Liu G. Y. (2008) Methane formation from $CaCO_3$ reduction catalyzed by high pressure. *Chinese Chem. Lett.* **19**, 475-478.

Clegg S. M., Barefield J. E., Wiens R. C., Quick C. R., Sharma S. K., Misra A. K., Dyar M. D., McCanta M. C., and Elkins-Tanton L. (2009) Venus geochemical analysis by remote Raman–laser induced breakdown spectroscopy (Raman-LIBS). Venus geochemistry: progress, prospects, and new missions, 26–27 February 2009, Gilruth Center, NASA Johnson Space Center, Houston, TX. LPI Contribution No. 1470, p. 12-13

Culler T. S. and Schiferl D. (1993) New chemical-reactions in methane at high-temperatures and pressures. *J. Phys. Chem.* **97**, 703-706.

Dussault D. and Hoess P. (2004) ICCDs edge out electron-multiplying CCDs in low light. *Laser Focus World* **40**, 69-76.

Dyar M. D., Agresti D. G., Schaefer M. W., Grant C. A., and Sklute E. C. (2006) Mössbauer spectroscopy of earth and planetary materials. *Annu. Rev. Earth Planet. Sci.* **34**, 83-125.

Erdogan T. and Mizrahi V. (2003) Thin-film filters come of age. *Photonics Spectra* **37**, 94-100.

Eremets M. I. and Trojan I. A. (2009) Evidence of maximum in the melting curve of hydrogen at megabar pressures. *JETP Letters* **89**, 174-179.

Fateley W. G. (1972) Infrared and Raman selection rules for molecular and lattice vibrations: The correlation method. New York: Wiley-Interscience.

Fries M. and Steele A. (2008) Graphite whiskers in CV3 meteorites. *Science* **320**, 91-93.

Fries M. and Steele A. Raman Spectroscopy and Confocal Raman Imaging in Mineralogy and Petrography. In *Confocal Raman Microscopy* (eds. T. Dieing, O. Hollricher, and J. Toporski). Springer Science, New York, pp.111-133.

Gao L., Chen B., Wang J., Alp E. E., Zhao J., Lerche M., Sturhahn W., Scott H. P., Huang F., Ding Y., Sinogeikin S. V., Lundstrom C. C., Bass J. D., and Li J. (2008) Pressure-induced magnetic transition and sound velocities of Fe_3C: implications for carbon in the earth's inner core. *Geophys. Res. Lett.* **35**, L17306.

Gerdau E., Rüffer R., Winkler H., Tolksdorf W., Klages C. P., and Hannon J. P. (1985) Nuclear Bragg diffraction of synchrotron radiation in yttrium iron garnet. *Phys. Rev. Lett.* **54**, 835-838.

Greenwood N. N. and Gibb T.C. (1972) Mössbauer Spectroscopy. Chapman and Hall, London.

Gillet P., Fiquet G., Danil I., and Reynard B. (1993) Raman-spectroscopy at mantle pressure and temperature conditions experimental set-up and the example of $CaTiO_3$ perovskite. *Geophys. Res. Lett.* **20**, 1931-1934.

Gillet P., Hemley R. J., and McMillan P. F. (1998) Vibrational properties at high pressures and temperatures. *Rev. Mineral.* **37**, 525-590.

Goncharov A. F., Gregoryanz E., Mao H. K., Liu Z., and Hemley R. J. (2000) Optical evidence for nonmolecular phase in nitrogen above 150 GPa. *Phys. Rev. Lett.* **85**, 1262-1265.

Goncharov A. F. and Struzhkin V. V. (2003) Raman spectroscopy of metals, high-temperature superconductors and related materials under high pressure. *J. Raman Spectrosc.* **34**, 532-548.

Goncharov A. F., Crowhurst J. C., Dewhurst J. K., and Sharma S. (2005a) Raman spectroscopy of cubic boron nitride under extreme conditions of high pressure and temperature. *Phys. Rev. B* **72**, 100104(R).

Goncharov A. F., Goldman N., Fried L. E., Crowhurst J. C., Kuo I. F. W., Mundy C. J., and Zaug J. M. (2005b) Dynamic ionization of water under extreme conditions. *Phys. Rev. Lett.* **94**, 125508.

Goncharov A. F. and Crowhurst J. C. (2005) Pulsed laser Raman spectroscopy in the laser-heated diamond anvil cell. *Rev. Sci. Instru.* **76**, 063905.

Goncharov A. F., Crowhurst J. C., Struzhkin V. V., and Hemley R. J. (2008) Triple point on the melting curve and polymorphism of nitrogen at high pressure. *Phys. Rev. Lett.* **101**, 095502.

Goncharov A. F., Montoya J. A., Subramanian N., Struzhkin V. V., Kolesnikov A., Somayazulu M., and Hemley R. J. (2009) Laser heating in diamond anvil cells: developments in pulsed and continuous techniques. *J. Synchrotron Rad.* **16**, 769-772.

Gregoryanz, E., Goncharov A. F., Matsuishi K., Mao H. K., and Hemley R. J. (2003) Raman spectroscopy of hot dense hydrogen. *Phys. Rev. Lett.* **90**, 175701.

Hawthorne F. C. (1988) Spectroscopic methods in mineralogy and geology, In *Review in Mineralogy: Spectroscopic Methods in Mineralogy and Geology* (ed. F. C. Hawthorne). Mineralogical Society of America.

Hemley R. J. (2000). Effects of high pressure on molecules. *Annu. Rev. Phys. Chem.* **51**, 763-800.

Hemley R. J. and Mao H. K. (2004) New findings in static high-pressure science. 13th APS Conference on Shock-compression of Condensed Matter, American Institute of Physics.

Hemley R. J. and Porter R. F. (1988) Raman spectroscopy at ultrahigh pressures. *Scripta Metall. Mater.* **22**, 139-144.

Hirai H., Konagai K., Kawamura T., Yamamoto Y., and Yagi T. (2009) Polymerization and diamond formation from melting methane and their implications in ice layer of giant planets. *Phys. Earth Planet. Inter.* **174**, 242-246.

Hsu H., Umemoto K., Blaha P., and Wentzcovitch R. M. (2010) Spin states and hyperfine interactions of iron in (Mg,Fe)SiO_3perovskite under pressure. *Earth Planet. Sci. Lett.* ***294***, 19-26.

Hu M. Y., Sturhahn W., Toellner T. S., Mannheim P. D. Brown D. E., Zhao J., and Alp E. E. (2003) Measuring velocity of sound with nuclear resonant inelastic x-ray scattering. *Phys. Rev.* B **67**, 094304

Iota, V., Yoo C. S., and Cynn H. (1999) Quartzlike carbon dioxide: An optically nonlinear extended solid at high pressures and temperatures. *Science* **283**, 1510-1513.

Iota, V., Yoo C. S., Klepeis J. H., Jenei Z., Evans W., and Cynn H. (2007) Six-fold coordinated carbon dioxide VI. *Nature Materials* **6**, 34-38.

Jackson J. M., Sturhahn W., Tschauner O., Lerche M., and Fei Y. (2009) Behavior of iron in (Mg,Fe)SiO_3 perovskite assemblages at Mbar pressures. *Geophys. Res. Lett.* **36**, L10301.

Jackson J. M., Hamecher E. A., and Sturhahn W. (2009) Nuclear resonant x-ray spectroscopy of (Mg.Fe)SiO_3 orthoenstatites. *Eur. J. Mineral.* **21**, 551-560.

Kaminsky F., Wirth R., Matsyuk S., Schreiber A., and Thomas R. (2009) Nyerereite and nahcolite inclusions in diamond: evidence for lower-mantle carbonatitic magmas. *Mineral. Mag.* **73**, 797-816.

Katayama I. and Maruyama S. (2009) Inclusion study in zircon from ultrahigh-pressure metamorphic rocks in the Kokchetav massif: an excellent tracer of metamorphic history. *J. Geol. Soc. London* **166**, 783-796.

Kenney J. F., Kutcherov V. A., Bendeliani N. A., and Alekseev V. A. (2002) The evolution of multicomponeint systems at high pressures: VI. The thermodynamic stability of the hydrogen-carbon system: The genesis of hydrocarbons and the origin of petroleum. *Proc. Natl. Acad. Sci. USA* **99**, 10976-10981.

Kim M., Owen H. Carey P. R. (1993) High-performance Raman-spectroscopic system based on a single spectrograph, CCD, notch filters, and a Kr^+ laser ranging from the near-IR to near-UV regions. *Appl. Spectrosc.* **47**, 1780-1783.

Kittel C. (1996) Introduction to Solid State Physics. John Wiley & Sons, New York, Chichester.

Klingelhöfer G., Morris R. V., Bernhardt B., Rodionov D., De Souza Jr. P. A., Squyres S. W., Foh J., Kankeleit E., Bonnes U., Gellert R., Schröder Ch., Linkin S., Evlanov E., Zubkov B., and Prilutski O. (2003) Athena MIMOS II Mössbauer spectrometer investigation. *J. Geophys. Res.* **108**, 8067.

Kobayashi H., Kamimura T., Alfè D., Sturhahn W., Zhao J., and Alp E. E. (2004) Phonon density of states and compression behavior in iron sulfide under pressure. *Phys. Rev. Lett.* **93**, 195503.

Kolesnikov, A., Kutcherov V. G., and Goncharov A. F. (2009) Methane-derived hydrocarbons produced under upper-mantle conditions. *Nat. Geosci.* **2**, 566-570.

Kress J. D., Bickham S. R., Collins L. A., and Holian B. L. (1999) Tight-binding molecular dynamics of shock waves in methane. *Phys. Rev. Lett.* **83**, 3896-3899.

Li J., Struzhkin V. V., Mao H. K., Shu J., Hemley R. J., Fei Y., Mysen B., Dera P., Prakapenka V., and Shen G. (2004) Electronic spin state of iron in lower mantle perovskite. *Proc. Natl. Acad. Sci. USA* ***101***, 14027-14030.

Lin J. F., Struzhkin V. V., Sturhahn W., Huang E., Zhao J., Hu M. Y., Alp E. E., Mao H. K., Boctor N., and Hemley R. J. (2003) Sound velocities of iron-nickel and iron-silicon alloys in the Earth's core. *Geophys. Res. Lett.* **30**, 2112.

Lin J. F., Santoro M., Struzhkin V. V., Mao H. K., and Hemley R. J. (2004a). *In situ* high pressure-temperature Raman spectroscopy technique with laser-heated diamond anvil cells. *Rev. Sci. Instrum.* **75**, 3302-3306.

Lin J. F., Sturhahn W., Zhao J., Shen G., Mao H. K., and Hemley R. J. (2004b) Absolute temperature measurement in a laser-heated diamond anvil cell. *Geophys. Res. Lett.* **31**, L14611.

Lin J. F., Fei Y., Sturhahn W., Zhao J., Mao H. K., and Hemley R. J. (2004c) Magnetic transition and sound velocities of Fe_3S at high pressure: applications for Earth and planetary cores. *Earth Planet. Sci. Lett.* **226**, 33-40.

Lin J. F., Gregoryanz E., Struzhkin V. V., Somayazulu M., Mao H. K., and Hemley R. J. (2005a) Melting behavior of H_2O at high pressures and temperatures. *Geophys. Res. Lett.* **32**, L11306.

Lin J. F., Sturhahn W., Zhao J., Shen G., Mao H. K., and Hemley R. J. (2005b) Sound velocites of hot dense iron: Birch's law revisited. *Science* **308**, 1892-1894.

Lin J. F., Struzhkin V. V., Jacobsen S. D., Hu M., Chow P., Kung J., Liu H., Mao H. K., and Hemley R. J. (2005c) Spin transition of iron in magnesiowüstite in Earth's lower mantle. *Nature **436***, 377-380.

Lin J. F., Gavriliuk A. G., Struzhkin V. V., Jacobsen S. D., Struhahn W., Hu M. Y., Chow P., and Yoo C. S. (2006) Pressure-induced electronic spin transition of iron in magnesiowustite-(Mg,Fe)O. *Phys. Rev. B* **73**, 113107.

Lin J. F., Jacobsen S. D., Sturhahn W., Jackson J. M., Zhao J., and Yoo C. S. (2007a) Sound velocities of ferropericlase in Earth's lower mantle. *Geophys. Res. Lett.* **33**, L22304.

Lin J. F., Vankó G., Jacobsen S. D., Iota V., Struzhkin V. V., Prakapenka V. B., Kuznetsov A., and Yoo C. C. (2007b) Spin transition zone in Earth's lower mantle. *Science* **317**, 1740-1743.

Lin J. F. and Tsuchiya T. (2008a) Spin transition of iron in the Earth's lower mantle. *Phys. Earth Planet. Inter.* **170**, 248-259.

Lin J. F., Watson H. C., Vankó G., Alp E. E., Prakapenka V. B., Dera P., Struzhkin V. V., Kubo A., Zhao J., McCammon C., and Evans W. J. (2008b) Intermediate-spin ferrous iron in lowermost mantle post-perovskite and perovskite. *Nat. Geosci.* ***1***, 688-691.

Lin J. F., Gavriliuk A. G., Sturhahn W., Jacobsen S. D., Zhao J., Lerche M., and Hu M. (2009) Synchrotron Mössbauer spectroscopic study of ferropericlase at high pressures and temperatures. *Am. Miner.* **94**, 594-599.

Long G. J. and Grandjean F. (eds). (1989) Mössbauer Spectroscopy Applied to Inorganic Chemistry, in Modern Inorganic Chemistry Volume, Plenum Pub Corp.

Lu R., Goncharov A., Mao H. K., and Hemley R. J. (1999) Synchrotron infrared microspectroscopy: applications to hydrous minerals. In Synchrotron X-ray Methods in Clay Science (eds. D. Schulze, J. W. Stucki and P. M. Bertsch). Boulder, CO, The Clay Minerals Society, **9**, pp. 165-182.

Mao H. K., Xu J., Struzhkin V. V., Shu J., Hemley R. J., Sturhahn W., Hu M. Y., Alp E. E., Vocadlo L., Alfè D., Price G. D., Gillan M. J., Schwoerer-Böhning M., Häusermann D., Eng P., Shen G., Giefers H., Lübbers R., and Wortmann G. (2001) Phonon density of states of iron up to 153 gigapascals. *Science* **292**, 914.

Mao W. L., Sturhahn W., Heinz D. L., Mao H. K., Shu J., and Hemley R. J. (2004) Nuclear resonant x-ray scattering of iron hydride at high pressure. *Geophys. Res. Lett.* **31**, L15618.

Mao Z., Lin J. F., Jacobs C., Watson H. C., Xiao Y., Chow P., Alp E. E., and Prakapenka V. B. (2010) Electronic spin and valence states of Fe in $CaIrO_3$-type post-perovskite in the Earth's lowermost mantle. *Geophys. Res. Lett.* **37**, L22304.

McCammon C., Kantor I., Narygina O., Rouquette J., Ponkratz U., Sergueev I., Mezouar M., Prakapenka V., and Dubrovinsky L. (2008) Stable intermediate-spin ferrous iron in lower-mantle perovskite. *Nat. Geosci.* ***1***, 684-687.

McCammon C., Dubrovinsky L., Narygina O., Kantor I., Wu X., Glazyrin K., Sergueev I., and Chumakov A. I. (2010) Low-spin Fe^{2+} in silicate perovskite and a possible layer at the base of the lower mantle. *Phys. Earth Planet. Inter.* ***180***, 215-221.

McMillan P. F. (1985) Vibrational spectroscopy in the mineral sciences. In *Microscopic to macroscopic: atomic environments to mineral thermodynamics* (eds. S. W. Kiffer and A. Navrotsky). **14**, pp. 9-63.

McMillan P. F. (1989) Raman spectroscopy in mineralogy and geochemistry. *Ann. Rev. Earth Planet. Sci.* **17**, 255-83.

McMillan P. F., Dubessy J., and Hemley R. J. (1996) Applications in earth, planetary and environmental sciences. In *Raman Microscopy, Development and Applications* (eds. G. Turrell G. and J. Corset). New York, Academic Press, 289-365.

Merkel S., Goncharov A. F., Mao H. K., Gillet P., and Hemley R. J. (2000) Raman spectroscopy of iron to 152 gigapascals: Implications for Earth's inner core. *Science* **288**, 1626-1629.

Misra A. K., Sharma S., Chio C. H., Lucey P. G., Lienert B. (2005) Pulsed remote Raman system for daytime measurements of mineral spectra. *Spectrochim. Acta* A **61**, 2281-2287.

Montoya J. A., Rousseau R. Santoro M., Gorelli F., and Scandolo S. (2008) Mixed threefold and fourfold carbon coordination in compressed CO_2. *Phys. Rev. Lett.* **100**, 163002.

Morris R. V., Ruff S. W., Gellert R., Ming D. W., Arvidson R. E., Clark B. C., Golden D. C., Siebach K., Klingelhöfer G., Schröder C., Fleischer I., Yen A. S., and Squyres S. W. (2010) Identification of carbonate-rich outcrops on Mars by the Spirit Rover. *Science* **329**, 421-242.

Moser, C. and Havermeyer F. (2009) Ultra-narrow-band tunable laserline notch filter. *Appl. Phys. B- Lasers O* **95**, 597-601.

Mössbauer R. L. (1958) Kernresonanzfluoreszenz von gammastrahlung in Ir^{191}. *Z. Physik* **151**, 124-143.

Mysen B. O. (2010) Speciation and mixing behavior of silica-saturated aqueous fluid at high temperature and pressure. *Am. Mineral.* **95**, 1807-1816.

Nellis W. J., Hamilton D. C., and Mitchell A. C. (2001). Electrical conductivities of methane, benzene, and polybutene shock compressed to 60 GPa (600 kbar). *J. Chem. Phys.* **115**, 1015-1019.

Nellis W. J., Ree F. H., Van Thiel M., and Mitchell A. C. (1981) Shock compression of liquid carbon-monoxide and methane to 90 GPa (900 Kbar). *J. Chem. Phys.* **75**, 3055-3063.

Nestola F., Nimis P., Ziberna L., Longo M., Marzoli A., Harris J. W., Manghnani M. H., and Fedortchouk Y. (2011) First crystal-structure determination of olivine in diamond: Composition and implications for provenance in the Earth's mantle. *Earth Planet. Sci. Lett.* **305**, 249-255.

Porto S. P. S., Fleury P. A.,and Damen T. C. (1967) Raman spectra of TiO_2, MgF_2, ZnF_2, FeF_2, and MnF_2. *Phys. Rev.* **154**, 522-526.

Pound R. V., Benedek G. B., and Drever R. (1961) Effect of hydrostatic compression on the energy of the 14.4-kev gamma ray from Fe^{57} in iron. *Phys. Rev. Lett.* 7, 405-408.

Prakapenka V. B., Kubo A., Kuznetsov A., Laskin A., Shkurikhin O., Dera P., Rivers M. L., and Sutton S. R. (2008). Advanced flat top laser heating system for high pressure research at GSECARS: application to the melting behavior of germanium. *High Pressure Res.* **28**, 225-235.

Raman, C. V. and Nedungadi T. M. K. (1940) The α-β transformation of quartz. *Nature* **145**, 147-147.

Ross M. (1981) The ice layer in Uranus and Neptune- diamonds in the sky. *Nature* **292**, 435-436.

Ruby S. L. (1974) Experiments without conventional sources. *J. Phys. Colloq.* **35**, C6-209.

Sage J. T., Paxson C., Wyllie G. R. A., Sturhahn W., Durbin S. M., Champion P. M., Alp E. E., and Scheidt W. R. (2001) Nuclear resonance vibrational spectroscopy of a protein active-site mimic. *J. of Phys: Cond. Matter* **13**, 7707.

Santoro M., Gorelli F. A., Bini R., Ruocco G., Scandolo S., and Crichton W. A. (2006) Amorphous silica-like carbon dioxide. *Nature* **441**, 857-860.

Santoro M., Lin J. F., Mao H. K., and Hemley R. J. (2004) *In situ* high P-T Raman spectroscopy and laser heating of carbon dioxide. *J. Chem. Phys.* **121**, 2780-2787.

Schiferl D., Buchsbaum S., and Mills R. L. (1985) Phase-transitions in nitrogen observed by Raman-spectroscopy from 0.4 to 27.4 GPa at 15 K. *J. Phys. Chem.* **89**, 2324-2330.

Scott H. P., Hemley R. J., Mao H. K., Herschbach D. R., Fried L. E., Howard W. M., and Bastea S. (2004) Generation of methane in the Earth's mantle: *In situ* high pressure-temperature measurements of carbonate reduction. *Proc. Natl. Acad. Sci. USA* **101**, 14023-14026.

Seto M., Masuda R., Higashitaniguchi S., Kitao S., Kobayashi Y., Inaba C., Mitsui T., and Yoda Y. (2009) Synchrotron-radiation-based Mössbauer spectroscopy. *Phys. Rev. Lett.* **102**, 217602.

Sharma S. K., Misra A. K., Clegg S. M., Barefield J. E., Wiens R. C., and Acosta T. (2010) Time-resolved remote Raman study of minerals under supercritical CO_2 and high temperatures relevant to Venus exploration. *Philos. T. Roy. Soc. A* **368**, 3167-3191.

Shenoy G. K. and Wagner F. E. (1978) Mössbauer Isomer Shifts. North-Holland Publishing Company.

Shim S., Lamm R., Rekhi S., Catalli K., Santillan J., and Lundin S. (2005) New micro-Raman spectroscopy systems for high-temperature studies in the diamond anvil cell. Eos Trans. AGU, 86(52), Fall Meet., Abstract MR13B-02.

Sobolev N. V., Fursenko B. A., Goryainov S. V., Shu J., Hemley R. J., Mao H. K., and Boyd F. R. (2000) Fossilized high pressure from the Earth's deep interior: The coesite-in-diamond barometer. *Proc. Natl. Acad. Sci. USA* **97**, 11875-11879.

Spanu L., Donadio D., Hohl D., Schwegler E., and Galli G. (2011) Stability of hydrocarbons at deep Earth pressures and temperatures. *Proc. Natl. Acad. Sci. USA* **108**, 6843-6846.

Speziale S., Milner A., Lee V. E., Clark S. M., Pasternak M. P., and Jeanloz R. (2005) Iron spin transition in Earth's mantle. *Proc. Natl. Acad. Sci.* ***102***, 17918-17922.

Struzhkin V. V., Mao H. K., Hu J., Schwoerer-Böhning M., Shu J., and Hemley R. J. (2001) Nuclear inelastic X-ray scattering of FeO to 48 GPa. *Phys. Rev. Lett.* **87**, 255501.

Steele A., Fries M. D., Amundsen H. E. F., Mysen B. O., Fogel M. L., Schweizer M., and Boctor N. Z. (2007) Comprehensive imaging and Raman spectroscopy of carbonate globules from Martian meteorite ALH 84001 and a terrestrial analogue from Svalbard. *Meteorit. Planet. Sci.* **42**, 1549-1566.

Steele A., McCubbin F. M., Fries M., Glamoclija M., Kater L., and Nekvasil H. (2010) Graphite in an Apollo 17 impact melt breccia. *Science* **329**, 51-51.

Sturhahn W., Toellner T. S., Alp E. E., Zhang X., Ando M., Yoda Y., Kikuta S., Seto M., Kimball C. W., and Dabrowski B. (1995) Phonon density of states measured by inelastic nuclear resonant scattering. *Phys. Rev. Lett.* **74**, 3832.

Sturhahn W. (2001) Phase problem in synchrotron Mössbauer spectropscopy. *Phys. Rev. B.* **63,** 094105.

Subramanian N., Goncharov A. F., Struzhkin V. V., Somayazulu M., and Hemley R. J. (2011) Bonding changes in hot fluid hydrogen at megabar pressures. *Proc. Natl. Acad. Sci. USA* **108**, 6014-6019.

Subramanian N., Struzhkin V. V., Goncharov A. F., and Hemley R. J. (2010) A virtual experiment control and data acquisition system for *in situ* laser heated diamond anvil cell Raman spectroscopy. *Rev. Sci. Instrum.* **81**, 093906-093911.

Tateno S., Hirose K., Ohishi Y., and Tatsumi Y. (2010) The structure of iron in Earth's inner core. *Science* **330**, 359-361.

Toellner T. S. (2000) Monochromatization of synchrotron radiation for nuclear resonant scattering experiments. *Hyperfine Interact.* **125**, 3-28.

Tarcea N., Frosch T., Rösch P., Hilchenbach M., Stuffler T., Hofer S., Thiele H., Hochleitner R., and Popp J. (2008) Raman spectroscopy- A powerful tool for *in situ* planetary science. *Space Sci. Rev.* **25**, 281-292.

Tedesco J. M., Owen H., Pallister D. M., and Morris M. D. (1993) Principles and spectroscopic applications of volume holographic optics. *Anal. Chem.* **65**, 441A-449 A.

Tschauner O., Mao H. K., and Hemley R. J. (2001) New transformations of CO_2 at high pressures and temperatures. *Phys. Rev. Lett.* **87**, 075701.

Turrell G. (1996). Characteristics of Raman microscopy. In *Raman Microscopy: developments and applications* (eds. G. Turrell J. and Corset). London, Elsevier Academic Press.

Wang A. (2009) Planetary Raman spectroscopic study for understanding Venus evolution history. In Venus geochemistry: progress, prospects, and new missions, 26–27 February 2009, Gilruth Center, NASA Johnson Space Center, Houston, TX, Abstract, no. 2003.

Wirth R., Vollmer C., Brenker F., Matsyuk S., and Kaminsky F. (2007) Inclusions of nanocrystalline hydrous aluminium silicate "Phase Egg" in superdeep diamonds from Juina (Mato Grosso State, Brazil). *Earth Planet. Sci. Lett.* **259**, 384-399.

Yamamoto J., Kagi H., Kawakami Y., Hirano N., and Nakamura M. (2007) Paleo-Moho depth determined from the pressure of CO_2 fluid inclusions: Raman spectroscopic barometry of mantle- and crust-derived rocks. *Earth Planet. Sci. Lett.* **253**, 369-377.

Yang B., Morris M. D., Owen H. (1991) Holographic notch filter for low-wavenumber Stokes and Anti-Stokes-Raman spectroscopy. *Appl. Spectrosc.* **45**, 1533-1536.

Yasuzuka T., Ishibashi H., Arakawa M., Yamamoto J., and Kagi H. (2009) Simultaneous determination of Mg# and residual pressure in olivine using micro-Raman spectroscopy. *J. Miner. Petrol. Sci.* **104**, 395-400.

Yoo C. S., Cynn H., Gygi F., Galli G., Iota V., Nicol M., Carlson S., Häuermann D., and Mailhiot C. (1999) Crystal structure of carbon dioxide at high pressure: "Superhard" polymeric carbon dioxide. *Phys. Rev. Lett.* **83**, 5527-5530.

Zallen R. (1974). Pressure-Raman effects and vibrational scaling laws in molecular-crystals - S_8 and As_2S_3. *Phys. Rev. B* **9**, 4485-4496.

Zerr A., Serghiou G., Boehler R., and Ross M. (2006) Decomposition of alkanes at high pressures and temperatures. *High Pressure Res.* **26**, 23-32.

Zhao J., Sturhahn W., Lin J. F., Shen G., and Mao H. K. (2004) Nuclear resonant scattering at high pressure and high temperature, *High Pressure Res.* **24**, 447-457.

Figure 1 The energy and momentum transfer relationship for representative spectroscopic techniques using photons, electrons and neutrons as incident sources. The SMS technique essentially imparts negligible momentum transfer, but can distinguish hyperfine interactions with neV energies. The NRIXS imparts all of the momentum the photon has, so the momentum transfer range shown here covers different isotopes. The inelastic X-ray scattering (IXS) region show a wide range of the Q-E transfers in synchrotron IXS experiments. The Raman spectroscopy measures the vibrational optical modes at infinite momentum transfer (Calas and Hawthorne, 1988; Alp *et al.*, 2011). RIXS: resonant IXS.

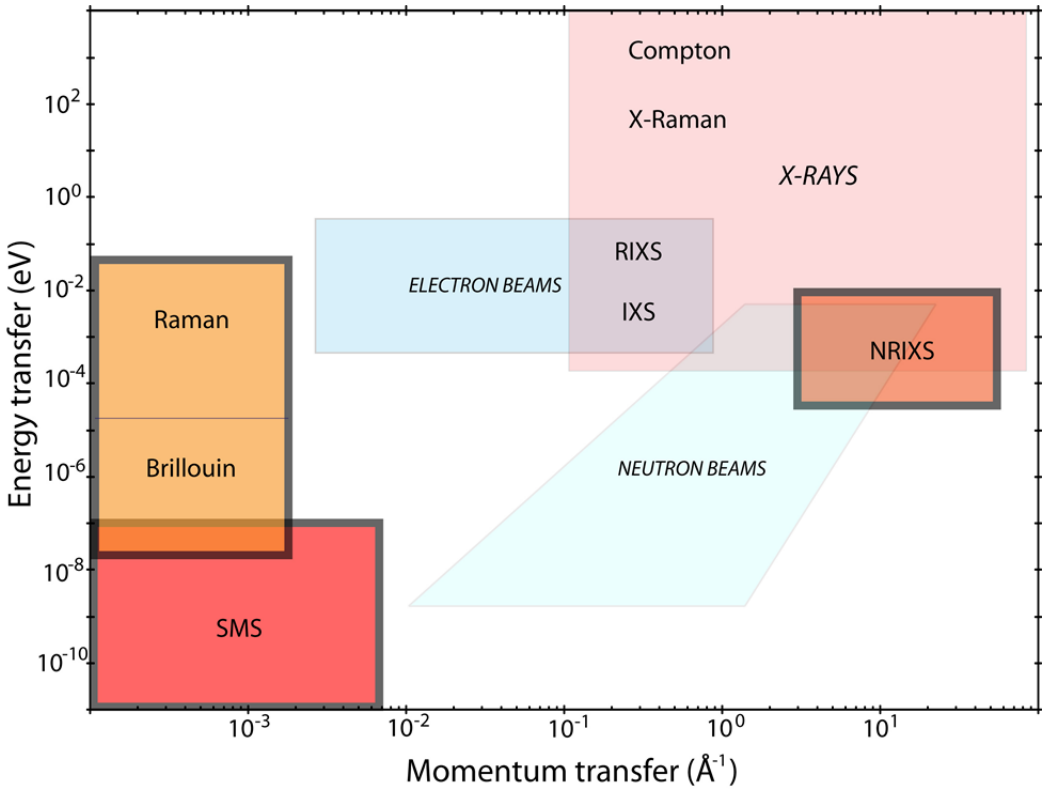

Figure 2 (a) Two representative *d*-orbital configurations in an octahedral site are shown to demonstrate the spatial organization of the ligands (black dots) with respect to the orbitals along the Cartesian axes. (b) Crystal field splitting diagram for metal ion in octahedral field. Energy is shown along the y-axis. All orbitals are raised to a uniform energy level in a spherically symmetric field. In an octahedral field, those orbitals lying in planes between axes are lower in energy than those that lie directly along the axes. Δ: crystal field splitting energy.

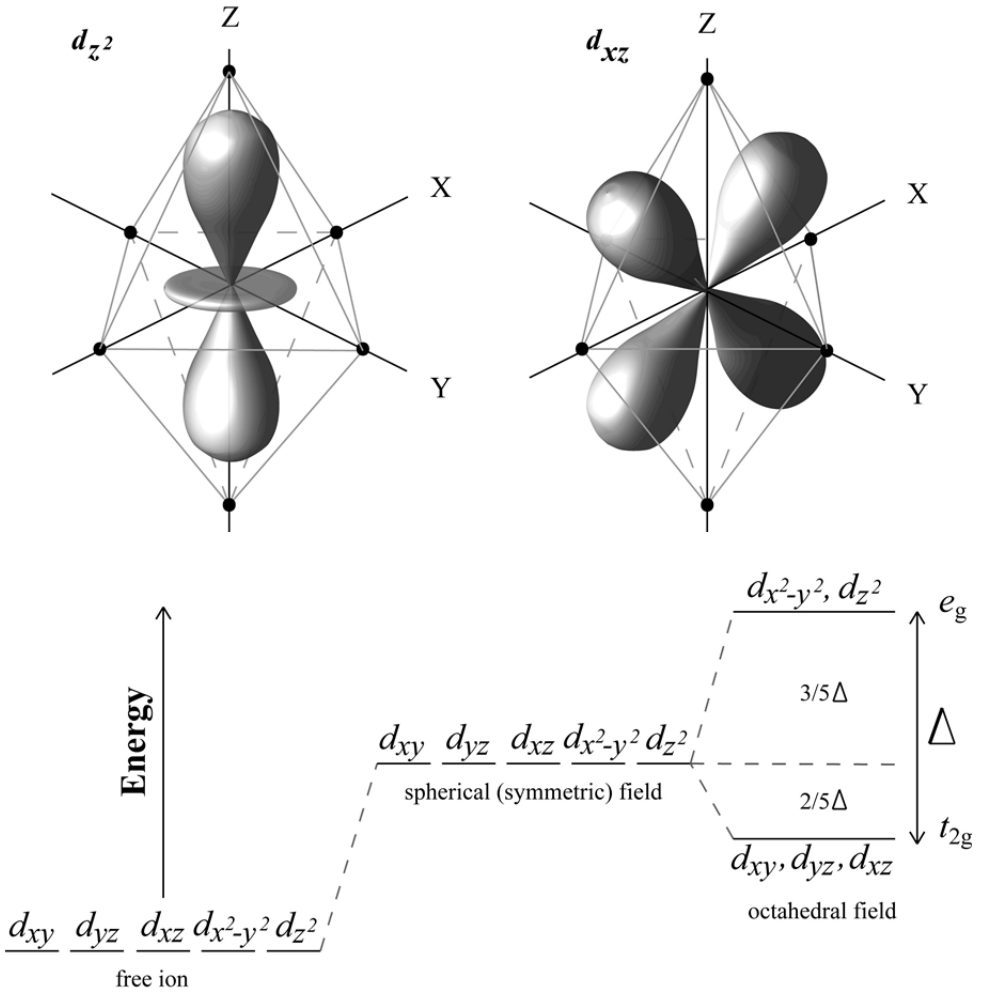

Figure 3 Representative map of the temperature distribution in the cavity of the diamond anvil cell determined in finite element calculations (Subramanian *et al.*, 2011). Left panel: Contour plot. Right panel: Temperature variation along the DAC axis. Red line in the contour plot is a boundary between fluid and solid phases.

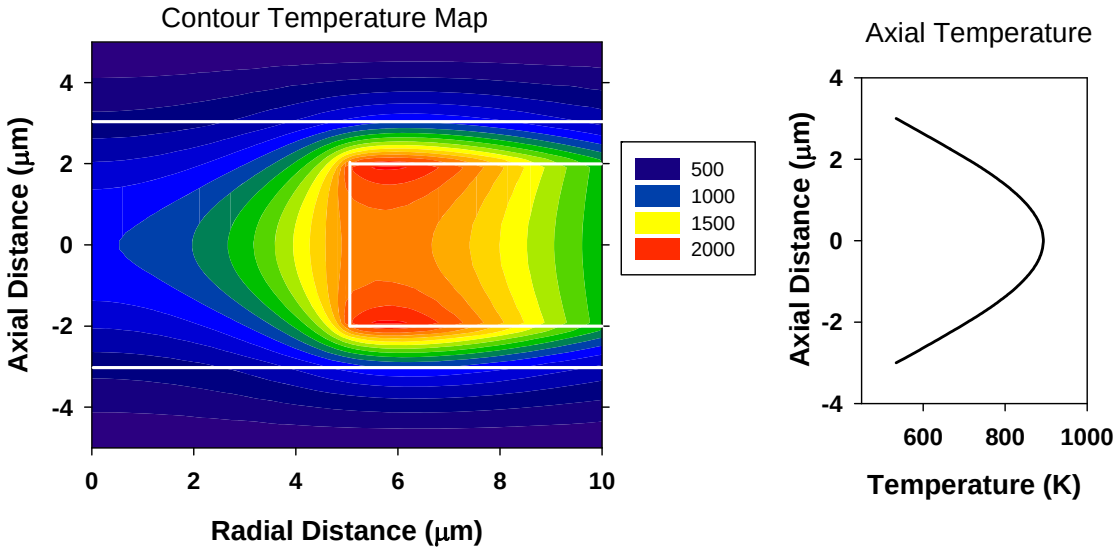

Figure 4 Schematic of the laser heating optical setup for Raman spectroscopy at Geophysical Laboratory of the Carnegie Institution of Washington (Goncharov *et al.*, 2009). Lower panel: sample configuration with respective to the laser beams in a DAC cavity.

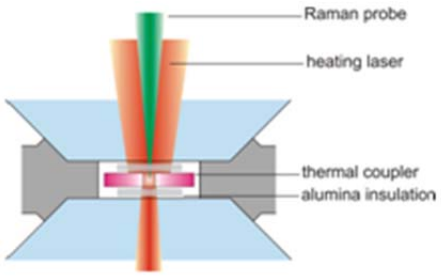

Figure 5 Identification of the chemical reaction products of laser heated methane at 2.5 and 5 GPa performed by *in situ* Raman spectroscopy in the DAC (Kolesnikov *et al.*, 2009).

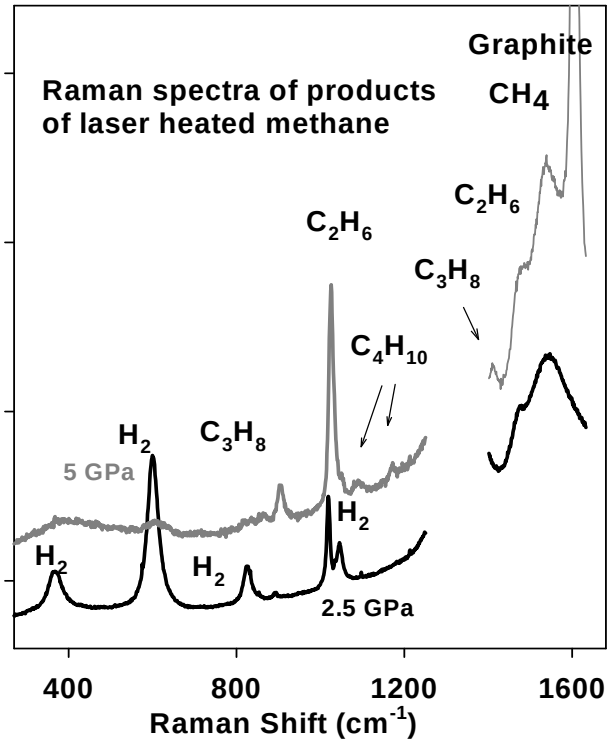

Figure 6 Classification of chemical (isomer) shifts and quadrupole splittings for ^{57}Fe isotope from 702 data records compiled by the Mössbauer Effect Data center (MEDC), showing demarcation regions for iron compounds with different valences (after Pound *et al.*, 1961).

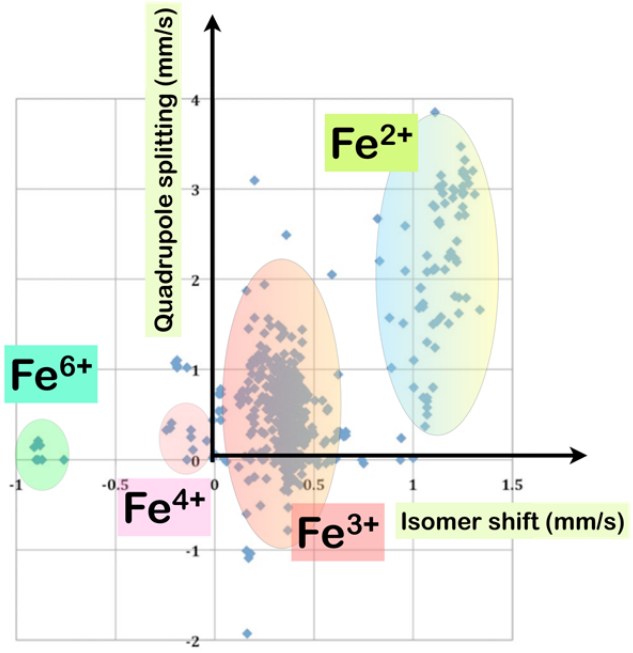

Figure 7 Classification of the chemical (isomer) shifts and quadrupole splittings for ^{151}Eu isotope from 216 data records compiled by the Mossbauer Effect data Center (MEDC), showing demarcation regions for iron compounds with different valences (after Greenwood and Gibb, 1972).

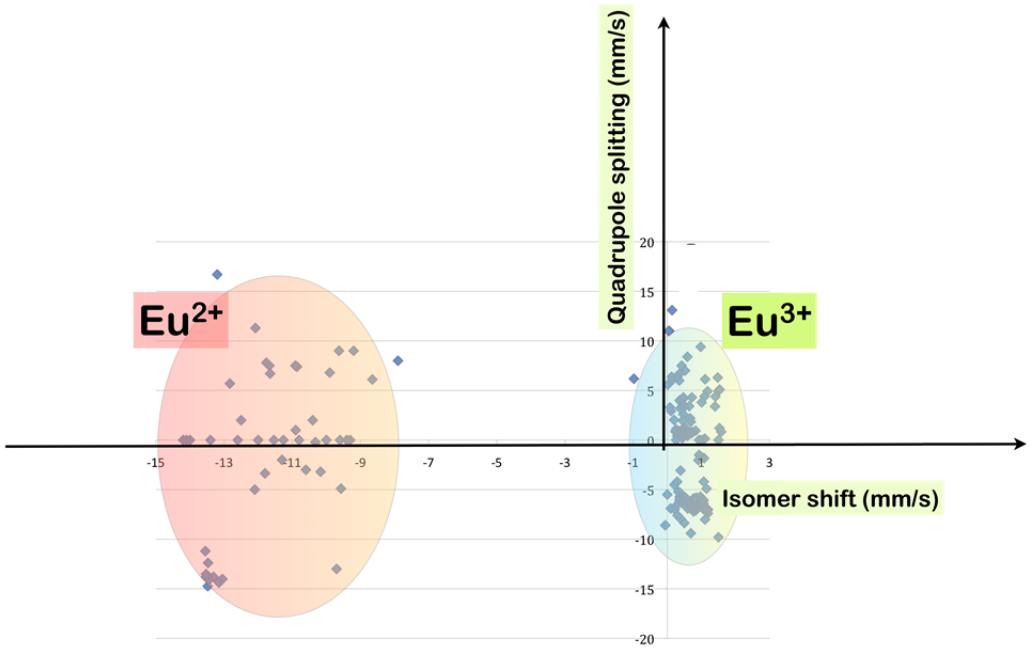

Figure 8 Basic elements of instrumentation for a conventional Mössbauer spectrometer system.

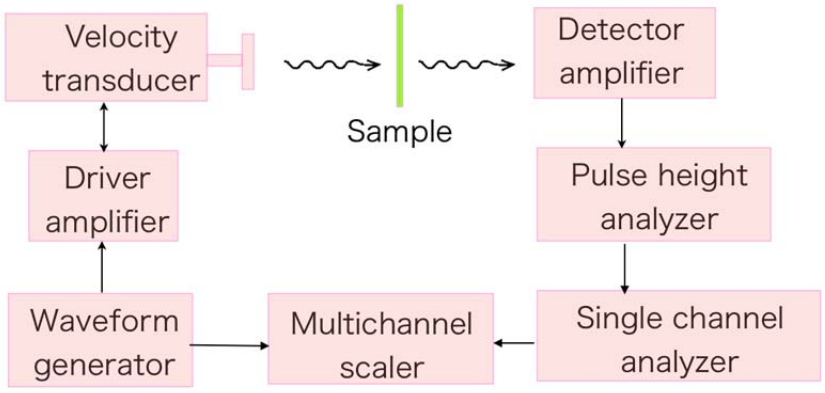

Figure 9 Basic elements of instrumentation for a synchrotron-based Mössbauer spectroscopy set-up.

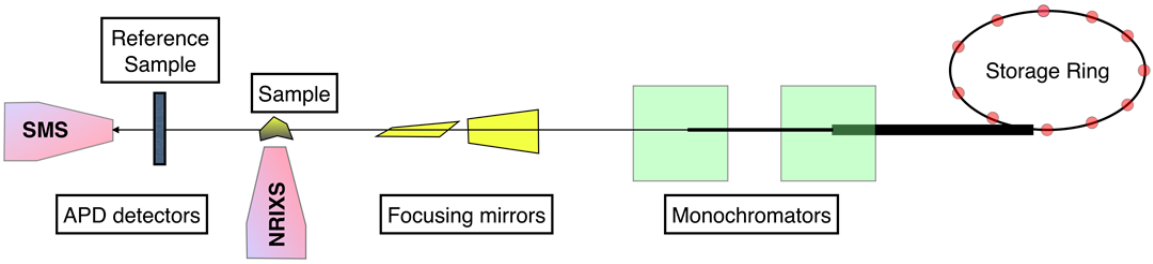

Figure 10 Typical data obtained from SMS (top panels) and from NRIXS measurements (middle and bottom panels). Measured NRIXS spectra (left panels) from kamacite and troilite phases in iron meteorites are used to derive the partial phonon DOS of iron (right panels) in the samples (Alp *et al*., unpublished).

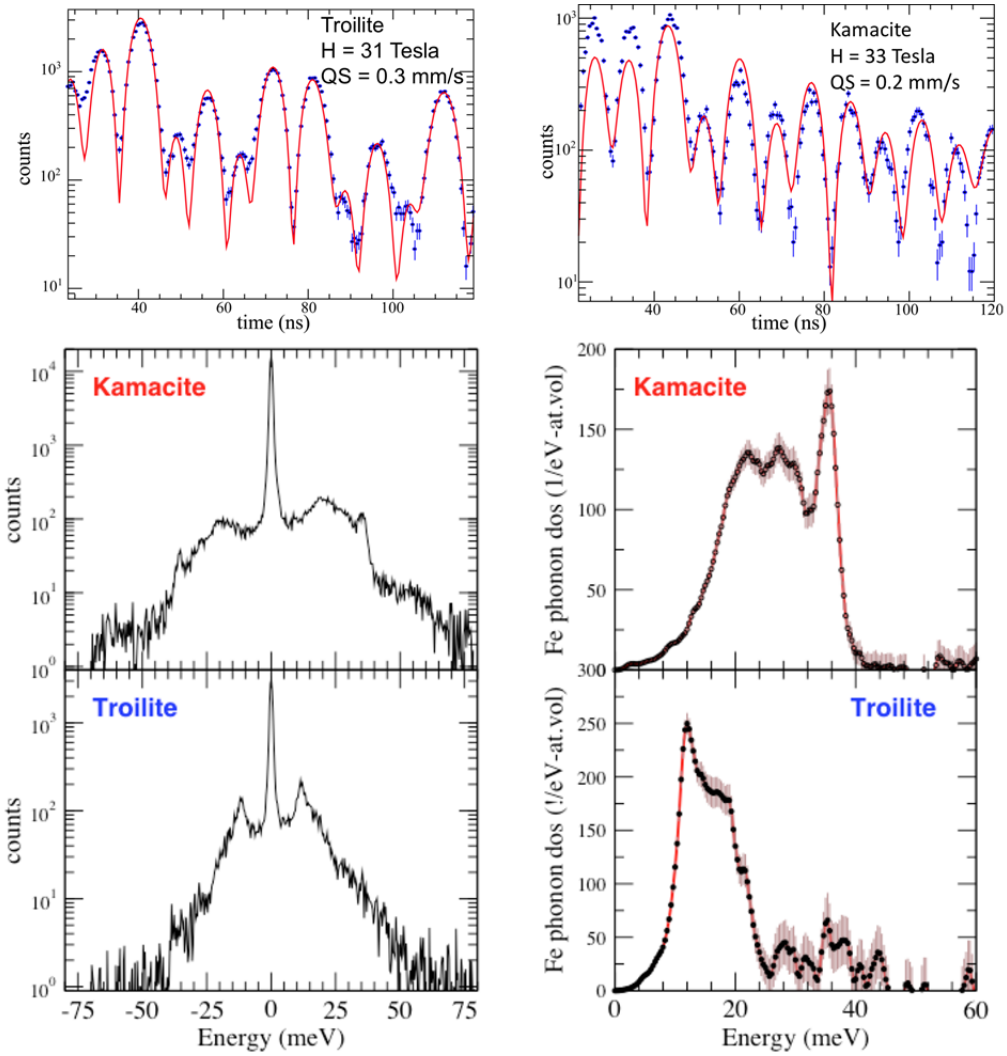

Table 1 Mössbauer transitions observed by synchrotron radiation given by their transition energies, half-lives, and first reported observations.

Isotope	Energy (keV)	Half-life (ns)	First published reference
^{181}Ta	6.2155	9800	A. I. Chumakov, et al, Phys. Rev. Lett. **75** (1995) 16384
^{169}Tm	8.4013	4	W. Sturhahn, et al, Europhys. Lett. **14** (1991) 821
^{83}Kr	9.4035	147	D.E. Johnson, et al, Phys. Rev. B **51** (1995) 7909
^{57}Fe	14.4125	97.8	E. Gerdau, et al, Phys.Rev.Lett. **54** (1985) 835
^{151}Eu	21.5414	9.7	O. Leupold, et al, Europhys. Lett. **35** (1996) 671
^{149}Sm	22.496	7.1	A. Barla, et al, Phys. Rev. Lett. **92** (2004) 066401
^{119}Sn	23.8794	17.8	E. E. Alp, et al, Phys. Rev. Lett. **70** (1993) 3351
^{161}Dy	25.6514	28.2	A. I. Chumakov, et al, Phys. Rev. B **63** (2001) 172301
^{201}Hg	26.2738	0.63	D. Ishikawa, et al, Phys. Rev. B **72** (2005) 140301
^{129}I	27.770	16.8	unpublished
^{40}K	29.834	4.25	M. Seto, et al, Hyperfine Interact. **141** (2002) 99
^{125}Te	35.460	1.48	H.C. Wille, et al, Europhys. Lett. **91** (2010) 62001
^{121}Sb	37.129	4.53	H.C. Wille, et al, Europhys. Lett. **74** (2006) 170
^{61}Ni	67.419	5.1	T. Roth, et al, Phys. Rev. B **71** (2005) 140401
^{73}Ge	68.752	1.86	M. Seto, et al, Phys. Rev. Lett. **102** (2009) 217602